STUDY AND DEVELOPEMENT OF WHIPSERING GALLERY MODE RESONATORS FOR TECHNOLOGICAL APPLICATIONS

Mathieu Couillard

A thesis
in
The Department
of
Physics

Presented in Partial Fulfillment of the Requirements
For the Degree of Master's of Science
Concordia University
Montréal, Québec, Canada

January 2021

Concordia University
School of Graduate Studies

This is to certify that the thesis prepared

By: **Mathieu Couillard**

Entitled: **Study and Developement of Whipsering Gallery Mode Resonators for Technological Applications**

and submitted in partial fulfillment of the requirements for the degree of

Master's of Science

complies with the regulations of this University and meets the accepted standards with respect to originality and quality.

Signed by the final examining commitee:

_____ Examiner

Dr.Ingo Salzmann

_____ Examiner

Dr.Valter Zazubovitz

_____ Supervisor

Dr.Pablo Bianucci

Approved _____

Dr.Valter Zazubovitz, Graduate Program Director

January 28, 2021 _____

Pascale Sicotte, Dean

Faculty of Arts and Science

Abstract

Study and Developement of Whipsering Gallery Mode Resonators for Technological Applications

Mathieu Couillard

Whispering gallery mode resonators (WGR) are optical cavities with very low loss. This property makes them particularly interesting for many applications including sensors and nonlinear optics. Despite all the research devoted to these cavities, many basic aspects of WGR are not completely understood and many issues still inhibit these technologies from being used in real world applications. This thesis aims to address some of these issues. First, this thesis presents an attempt of a non-destructive techniques to accurately measure the absolute radius and refractive index of a WGR. In order to do so, instrumental techniques were developed to first accurately determine the mode order number without relying on approximations and, second, determine the axial position where the radius is being measured. Perturbations of the modes are then studied using the interactions of a tapered fiber and optically trapped nanoparticle. An earlier experiment demonstrated a frequency shift occurs when the nanoparticle is in proximity of the tapered fiber. This effect was not observed in our experiment. This thesis then reviews the Pound-Drever-Hall technique and describes an implementation using a single board computer for many of the electrical components. Lastly, packaging was developed to improve the robustness of the tapered fiber and reverse the degradation of the Q factor due to adsorbed water on the surface of silica SNAPs. The packaging is robust enough to transport the fiber to different laboratories but cannot withstand the temperatures required to remove the adsorbed water.

Acknowledgments

I would like to first thank Professor Pablo Bianucci for his support which started a couple year before starting the Master's program. Since that time, he has guided me through my studies while granting me the freedom to explore the topics that interest me. I have learned many invaluable skills and techniques specifically about whispering gallery mode resonators and more generally across experimental physics. I also thank him for the many discussions we had which often led to insights and solutions to problems. Lastly, I thank him for suggesting and encouraging me to apply to the JSPS internship which had an undeniable effect on my career.

I would like to thank everyone involved in my work at Concordia University. Specifically, I would like to thank my labmates Samar Deep, Tabassom Hamidfar, Rajni Bagga, Kathleen McGarvey, Alexis Hotte-Kilburn, Mohammad Mirjalili and Mohammad Javad Safdari for the many discussions we had over the years. Furthermore, I would like to give a special thanks to Matthew Storms who gave me much of his time to discuss matters related to my courses and research.

I would like to thank the members of the Light Matter interaction Unit at the Okinawa Institute of Science and Technology(OIST). A special thanks goes to Professor Sile Nic Chormaic for providing an environment that gave me the resources and freedom to work on the topics that interested me. Secondly, to Doctor Jonathan Ward for the many discussion and for the opportunity to work alongside and learn from his experience.

Outside of research, I would like to thank Kathleen McGarvey and Amanda Spilkin for helping organize many of the Graduate Physics Association events. I would also like to thank my friends from McGill University Alexander Tychonick, Marco David with whom I enjoyed working with during our courses and at the McGill Physics Hackathon.

I would like to thank all those who offered me help after my apartment building

caught fire. Especially, Shubham Bhagat, Alex Glass, Vickie Vainionpaa and Ernest Lo for offering me a place to stay while I searched for a new apartment.

There are two friends I became particularly close to at Concordia. The first is Matthew Storms, I thank him for all the fun times exploring the Plateau-Mont-Royal, and all the fun conversations that ranged over math, physics, language, culture, philosophy and poetry. The second is Amanda Spilkin, I am grateful for all lunches in the park, coffee breaks and drinks at various locations around Montreal. At OIST I would like to highlight my friendships with Zhilin 'Ella' Liang, Theodoros Bouloumis and Celia Gonzalez Sanchez. It is with them I made the most enjoyable memories in Okinawa from camping near Cape Hedo to the 10,000 Eisa Dancers Parade in Naha. Outside of academia, I would like to thank my long time friends Firas Msaddi, Alex Glass and Nicholas Grenier. We have shared many memories together at countless gatherings and events.

Lastly, I would like to thank my father Patrice, mother Paula and brother Alexandre. Your love and support has been invaluable in the pursuit of this this degree as it has been throughout my life.

Contents

List of Figures

List of Tables

Chapter 1

Introduction

Over the past century, electronics have transform society, improving many aspects of life ranging from entertainment to life saving medical equipment and world communication. As revolutionary as these technologies were, they have certain limitation in which other platforms are better suited. One alternate is photonics, which has improved on the shortcomings of electronics in many fields including telecommunication[1], LIDAR[2], gyroscopes[3, 4] and atomic clocks[5], to name a few.

Electronics have often been improved by increasing the frequency range at which they operate. By shortening the period, the frequency can me measured in a shorter time. However, this has restricted electronics to the radio frequencies because as frequencies are increased into the terahertz range, the material losses attenuate the signal beyond practicality.

In contrast to guiding electromagnetic fields by current in metallic wires, photonics guide light through a dielectric using total internal reflection. By using photonics, much higher frequencies can be used with less attenuation[1]. These two properties were key in proliferation of fiber optic telecommunication in which the current record transmission rate has reached 178.08 Tbit/s [6].

One component which has shown promising results for photonics technologies is the whispering gallery mode resonator (WGR). These resonators consist of a circular dielectric in which light reflects by total internal reflection, as shown in Figure 1.1. When light is continuously pumped into the cavity, the light will circulate around the resonator and interfere with the light entering the cavity after one round trip. Due to the high frequency and low losses, light will build up, and store the energy in the

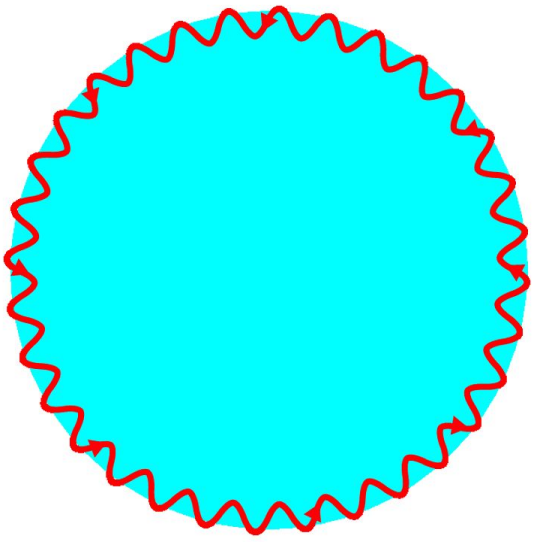

Figure 1.1: Light propagating around a circular dielectric by total internal reflection. Due to the circular shape, the light will circulate in a closed loop, producing a cavity.

optical fields for a long period of time.

Assuming the volume is sufficiently small, this build up allow physical phenomena, usually restricted by large threshold powers, to be observed using modest source power. Some examples of observed phenomena include non-linear optics[7, 8], nanoparticle trapping[9, 10], stimulated Raman scattering[11] and stimulated Brillouin scattering[12].

A second consequence of the high frequency and low loss is the narrow resonance peaks. These peaks are useful because the resonance wavelength an be more accurately measured. Since the resonance wavelength is dependent on many physical phenomena, WGR can behave as accurate sensors. Some examples of sensors include temperature[13–16], pressure[17–20], rotation[21–23], single nanoparticles[24–26], , electromagnetic field[27, 28], and gases[29–32]

This thesis focuses on surface nanoscale axial photonic (SNAP) resonator. A particular WGR which is characterized by its small radius variation in the out-of-plane direction of the circular path, as shown in Figure 1.2 a). This variation confines the light in 3 dimensions while allowing the light to slowly reflect back and forth, along the axis, to produce a standing wave along the axis. This property of slow light is a very active field of research with applications in optical switches[33], delay lines[34] and optical quantum memory[35].

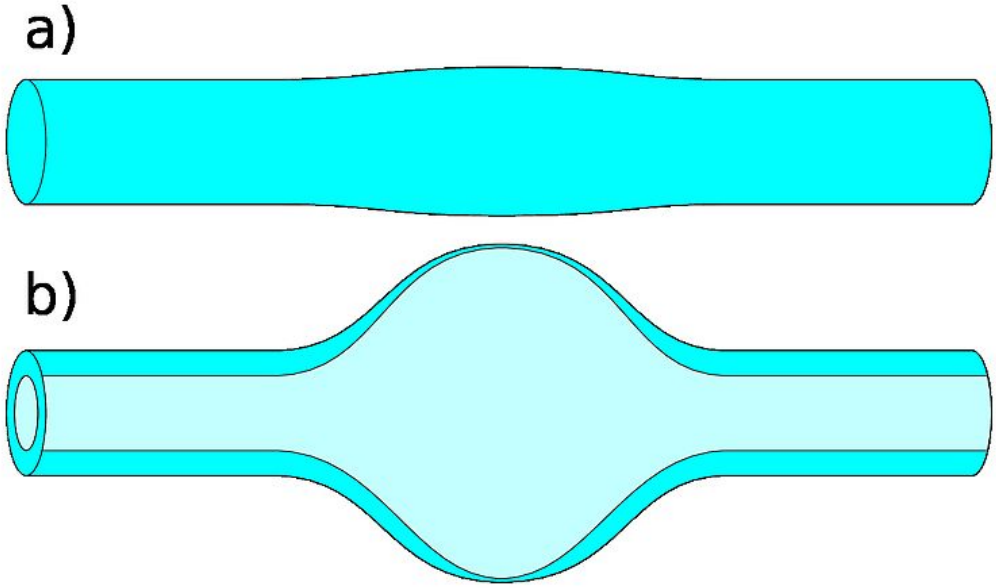

Figure 1.2: a) A SNAP resonator characterized by its small radius variation. Due to the slowly changing radius, the potential felt by the light will move it slowly along the axis in comparison to most other WGR. b) A microbubble with a hollow core that allows fluids to be sent though and interact with the light.

A second type of WGR on which this thesis focuses are microbubble. Microbubbles can be recognized by their hollow interior as seen in Figure 1.2 b). Similarly to SNAPs, variations in the radius confine the light in 3 dimensions. However, these WGR are interesting because the hollow interior can be filled with fluids to interact with the light. These resonators have shown to have many applications in nanoparticle detection[16], nanoparticle trapping[10]pressure sensors[20] and temperature sensors[16] among others.

Despite all the progress made, there are still a number of improvements needed before WGR's can be used in every day applications. The goal of this thesis is to address some of these issues. First, by developing precise measurement techniques that accurately determines the radius and refractive index of a SNAP. Secondly by studying the perturbation of the mode through the interaction of the tapered fiber and a nanoparticle. Lastly, to develop some packaging that can improve robustness while removing impurities that bind to the surface.

Chapter Overview and Collaborative Work

An general description of each chapters is given in this section. Many parts of the work for this thesis depended on previous work and collaboration with colleagues and supervisors.

Chapter 2 presents the basic concepts for understanding WGR and SNAPs which will be relevant to the other chapters. A derivation of the modes, Q factor, loss mechanisms, evanescent fields, cavity transfer function and coupling regimes is presented.

Chapter 3 describes a procedure to measure the refractive index and radius of a SNAP. It also describes the fabrication of SNAPs, tapered fiber and the experimental setup. The hardware for the experimental setup was built by Dr Tabassom Hamidfar while the program used for data collection were written in part by Matias Rittatore, Pablo Bianucci and the Author.

Chapter 4 describes an attempt to measure a resonance shift in a microbubble, when a nanoparticle, in an optical carousel trap, was near the tapered fiber. The chapter begins with the theory of nanoparticle trapping, nanoparticle detection, and describes how the hollow core and more spherical geometry modified the modes. This work was carried out at the Okinawa Institute of Science and Technology, with the Light Matter Interaction Unit as part of the JSPS-Mitacs Summer Program in partnership with SOKENDAI. The project was supervised by Prof. Sile Nic Chormaic and Staff Scientist Dr. Jonathan Ward. Much of the experimental setup and was built by Ward.

Chapter 5 describes a Pound-Drever-Hall lock to be used in subsequent experiment This lock will help increase the resolution of our measurements which is help measure very small variations in wavelength. This project was part of a collaboration with One Silicon Chip Photonics through an NSERC Engage grant with the goal of building a prototype optical gyroscope.

Chapter 6 describes the fabrication of packaging for a SNAP and taper system. The chapter also includes a description the testing of the device against impact and attempts to reverse the effects of the quality(Q) factor degradation.

Chaper 7 discussed the results and future work. It proposes a method to simultaneously sense changes in two physical phenomena, methods to increase improve the detection of the nanoparticle near the tapered fiber and how to overcome the limitations of our packaging.

Chapter 2

Surface Nanoscale Axial Photonic Resonators

This chapter introduces the theory of SNAPs and important concepts that will be need to understand the subsequent chapters. We start by describing the electromagnetic modes in a whispering gallery mode resonator. These modes describe the time independent fields on resonance. Next the quality (Q) factor, its relation to loss mechanisms and how it affects the modes are presented. Following this is a derivation of evanescent fields, and a discussion of mode coupling. The chapter continues with a derivation of the amplitude of the fields inside the cavity and the transfer function, defined as change in the light's field amplitude and phase due to the cavity. Finally, three different coupling regimes as discussed.

2.1 Maxwell's Equations

We start with Maxwell's equations for a linear, homogeneous, isotropic, and source free material. Using SI units, Maxwell's equations are

$$\boldsymbol{\nabla} \cdot \mathbf{D} = 0 \qquad \boldsymbol{\nabla} \cdot \mathbf{B} = 0 \tag{2.1}$$

$$\boldsymbol{\nabla} \times \mathbf{E} = -\frac{\partial \mathbf{B}}{\partial t} \qquad \boldsymbol{\nabla} \times \mathbf{H} = \frac{\partial \mathbf{D}}{\partial t}. \tag{2.2}$$

E is the electric field, H is the magnetic field, D is the electric displacement and B is the magnetic inductance. $\mathbf{E}$ is related to $\mathbf{D}$ and $\mathbf{H}$ is related to $\mathbf{B}$ by the constitutive

relations:

$$\mathbf{D} = \epsilon \mathbf{E} \qquad\qquad \mathbf{B} = \mu \mathbf{H}. \tag{2.3}$$

Where ϵ and μ are the permittivity and permeability of the medium, respectively. We now take the curl of the Ampere and Faraday's laws and substitute the constitutive relations to express everything in terms of the $\mathbf{E}$ and $\mathbf{B}$

$$\boldsymbol{\nabla} \times \boldsymbol{\nabla} \times \mathbf{E} = -\boldsymbol{\nabla} \times \frac{\partial \mathbf{B}}{\partial t} \qquad\qquad \boldsymbol{\nabla} \times \boldsymbol{\nabla} \times \frac{\mathbf{B}}{\mu} = \boldsymbol{\nabla} \times \frac{\partial \epsilon \mathbf{E}}{\partial t}. \tag{2.4}$$

On the left hand side of both equations, we use the vector calculus identity $\boldsymbol{\nabla} \times \boldsymbol{\nabla} \times \mathbf{A} = \boldsymbol{\nabla}(\boldsymbol{\nabla} \cdot \mathbf{A}) - \nabla^2 \mathbf{A}$ where the divergence terms are zero due to Gauss's law and its magnetic analog. On the right hand side, the differentials can be interchanged, and we assume the permittivity and permeability to be constant (low power and small wavelength range)

$$\nabla^2 \mathbf{E}, = -\frac{\partial \boldsymbol{\nabla} \times \mathbf{B}}{\partial t} \qquad\qquad \frac{1}{\mu} \nabla^2 \mathbf{B} = \epsilon \frac{\partial \boldsymbol{\nabla} \times \mathbf{E}}{\partial t}. \tag{2.5}$$

Using Ampere's law, Faraday's laws and the constitutive relations we obtain 2 wave equations

$$\nabla^2 \mathbf{E} = \frac{1}{\epsilon \mu} \frac{\partial^2 \mathbf{E}}{\partial t^2} \qquad\qquad \nabla^2 \mathbf{B} = \frac{1}{\epsilon \mu} \frac{\partial^2 \mathbf{B}}{\partial t^2}. \tag{2.6}$$

Where $\epsilon \mu = 1/v^2$ is the speed of light in the medium. Since the two equations have identical form, the solutions will also have the same form. From this point on, we only solve for the electric field equation and assumed the magnetic field has an analogous solution. Noticing that the temporal variable is separated on the right hand side of (2.6) we can identify the time dependence as

$$\mathbf{E} = \mathbf{E}_r(\mathbf{r}) e^{i\omega t}. \tag{2.7}$$

Inserting this in the wave equation and dividing by $\mathbf{E}$ yields

$$\nabla^2 \mathbf{E}_r(\mathbf{r}) = -k^2 \mathbf{E}_r(\mathbf{r}). \tag{2.8}$$

Where $k^2 = \mu \epsilon \omega^2$ is defined as the magnitude squared the wave vector.

2.2 Normal Modes

The normal modes are the spacial solution of the electric field everywhere inside the resonator for the time harmonic solution. We follow the derivations done by Louyer[36] and Bianucci[37], with a modification to include modes that propagate farther from the surface. We make one approximation in this derivation which is that the radius variation along the fiber is small enough that the SNAP can be treated as a cylinder.

2.2.1 Separation of Variables

Due to the cylindrical symmetry, we look for a solution in cylindrical coordinates as described in Figure 2.1. The electric field for the transverse electric (TE) mode, where the transverse direction points along the SNAP's axis, is assumed to have the form

$$\mathbf{E}(\mathbf{r}) = F(r,z)\Phi(\phi)Z(z)\hat{\mathbf{z}}. \tag{2.9}$$

Where $F(r,z)$ is the quasi-radial function, $\Phi(\phi)$ is the azimuthal function and $Z(z)$ is the axial function. Entering this solution into (2.8), we obtain

$$\frac{1}{rF(r,z)}\frac{\partial}{\partial r}\left(r\frac{\partial F(r,z)}{\partial r}\right) + \frac{1}{\Phi(\phi)r^2}\frac{\partial^2\Phi(\phi)}{\partial\phi^2} + \frac{1}{F(r,z)Z(z)}\frac{\partial^2(F(r,z)Z(z))}{\partial^2 z} = -k^2(z). \tag{2.10}$$

Due to the radial dependency on the last term of the left hand side, the differential equation is only separable in the approximation that the dependency is small. Typically, the radius variation is about 5 orders of magnitude less than the variation along the axis, as seen in Figure 2.1. Explicitly we assume, $Z\mathrm{d}^2F/\mathrm{d}z^2 \ll (\mathrm{d}Z\mathrm{d}F)/\mathrm{d}z^2 \ll F\mathrm{d}^2Z/\mathrm{d}z^2$ and the smaller terms can be ignored. The differential equation then reduces to

$$\frac{1}{rF(r)}\frac{\partial}{\partial r}\left(r\frac{\partial F(r)}{\partial r}\right) + \frac{1}{\Phi(\phi)r^2}\frac{\partial^2\Phi(\phi)}{\partial\phi^2} + \frac{1}{Z(z)}\frac{\partial^2(Z(z))}{\partial^2 z} = -k^2(z). \tag{2.11}$$

We start by separating the ϕ dependent term

$$\frac{1}{\Phi(\phi)}\frac{\partial^2\Phi(\phi)}{\partial\phi^2} = -m^2. \tag{2.12}$$

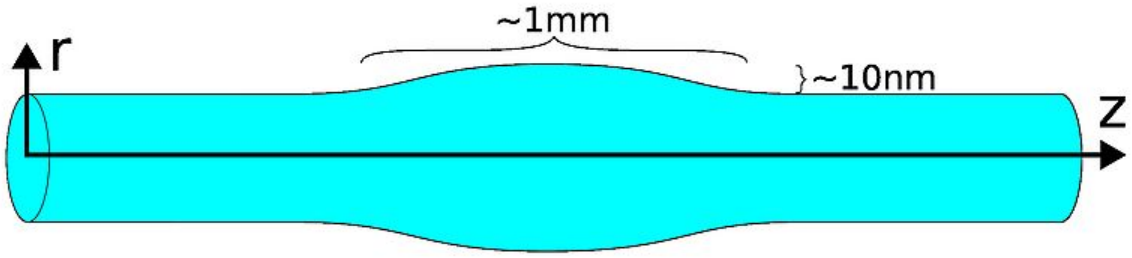

Figure 2.1: A SNAP, the cylindrical symmetry and nanoscale radius variations provide 3 dimensional confinement.

where m is the separation constant and represents all the terms in Equation (2.11) independent of ϕ, multiplied by r^2. Using periodic boundary conditions we recognize this as a sinusoidal function where m must be an integer.

$$\Phi(\phi) = e^{im\phi}. \tag{2.13}$$

Plugging (2.12) back into Equation (2.11) and rearranging

$$\frac{1}{F(r)}\frac{\partial^2 F(r)}{\partial r^2} + \frac{1}{F(r)r}\frac{\partial F(r)}{\partial r} + \left(k_\perp^2(z) - \frac{m^2}{r^2}\right) = -\frac{1}{Z(z)}\frac{\partial^2 Z(z)}{\partial z^2} + \left(k_\perp^2(z) - k^2\right), \tag{2.14}$$

where $k_\perp(z)$ is the magnitude of the wave vector perpendicular to the axis. It is added to the separation constant to make both sides equal to zero, where $k_\perp^2(z) - m^2/r^2 = k_r^2$ on the left hand side and $k_\perp^2(z) - k^2 = -k_z^2$ on the right hand side. k_r and k_z are the radial and axial components of the wave vector, respectively. These two sides do not completely separate due to the z dependence of $k_\perp$, which must be included to account for the change in radius along the axial direction. To show that $k_\perp$ is approximately constant, we note that $k_r/k_z = (\mathrm{d}F/\mathrm{d}z) \ll 1$[36] which is approximately true as long as the separation of variables is valid. The z dependence of the $k_\perp$ can be found by conservation of angular momentum. At any point along the fiber, the azimuthal number is $k_\perp R_{eff}(z) = m$ where $R_{eff}(z)$ is the effective radius. This can be thought of as the the radius corresponding to the same angular momentum if the field was completely located, as a Dirac delta function, at the SNAP-air interface. This effective radius differs from the physical radius of the SNAP because the modes are fields with an average radius inside the resonator. Using the cylindrical symmetry, we define the

relation $R(z) = fR_{eff}(z)$ to relate it to the physical radius, where f will be solved for after applying the interface conditions. We now have

$$k_{\perp}(z) = f\frac{m}{R(z)}. \tag{2.15}$$

Substituting the left hand side of (2.14) to zero and substituting (2.15) we obtain

$$\frac{\partial^2 Z(z)}{\partial z^2} = \left[f^2\frac{m^2}{R(z)^2} - k^2\right] Z(z). \tag{2.16}$$

We need to define the radius profile to find modes. For this example we specify $1/R^2(z) = [1 + (\alpha z)^2]/R_0^2$ for a maximum radius R_0 at the center and small perturbation from a cylinder, by the constant α. After rearranging we have

$$-\frac{\partial^2 Z(z)}{\partial z^2} + \left(\frac{fm\alpha z}{R_0}\right)^2 Z(z) = \left(k^2 - f^2\frac{m^2}{R_0^2}\right) Z(z). \tag{2.17}$$

We see that this choice of radius profile gives an equation with the same form as the quantum harmonic oscillator. In analogy, we define $E = k^2 - (fm)^2/R_0^2$ and $V = (\Delta E_m z/2)^2$ where $\Delta E = 2fm\alpha/R_0$. The solution to this equation is the Hermite-Gauss function,

$$Z_{mq}(z) = C_{mq}H_q\left(\sqrt{\frac{\Delta E_m}{2}}z\right)e^{-\frac{\Delta E_m}{4}z^2}. \tag{2.18}$$

Where q is the axial mode number, which indicated the number of field extrema in the standing wave along the axis, $C_{mq} = \sqrt[4]{\Delta E_m/[\pi 2^{2q+1}(q!)]^2}$ is the normalization factor and $H_q(x)$ is the hermite polynomial of degree q.

The axial component of the wave vector at the center is given by

$$k_z^2 = \left(q + \frac{1}{2}\right)\Delta E. \tag{2.19}$$

The right hand side of Equation (2.14) can be identified as Bessel's equation.

$$\frac{\partial^2 F(r)}{\partial r^2} + \frac{1}{r}\frac{\partial F(r)}{\partial r} + m^2\left(\frac{f^2}{R(z)^2} - \frac{1}{r^2}\right)F(r) = 0 \tag{2.20}$$

where the substitution of Equation (2.15) was made.
The solutions to this equation are

$$F(r) = \begin{cases} A_m J_m(k_\perp r) & , r \leq R(z) \\ B_m H_m^{(2)}(k_\perp r/n) & , r > R(z) \end{cases} \tag{2.21}$$

where $J_m(k_\perp r)$ is the cylindrical Bessel functions of first kind and $H_m^{(2)}(k_\perp r)$ is the Hankel functions of second kind. A_m and B_m are respectively real and complex coefficients which are related by applying the electromagnetic interface conditions. Their ratio at the interface is given by [38]

$$\frac{A_m}{B_m} = \frac{H_m^{(2)}(k_\perp R(z)/n)}{J_m(k_\perp R(z))} \tag{2.22}$$

One of the coefficients will vary with the field amplitude. We are now in a position to find the effective radius which will give f and therefore the modes' wave number. We compute the same ratio using the continuity of the first derivative of the fields and equate the two to remove all reference to the coefficients and obtain the transcendental equation(TEq) [38].

$$P\frac{((k_\perp R)^{1/2} J_m(k_\perp R))'}{(k_\perp R)^{1/2} J_m(k_\perp R)} = \frac{((k_\perp R/n)^{1/2} H_m(k_\perp R/n))'}{(k_\perp R/n)^{1/2} H_m(k_\perp R/n)}. \tag{2.23}$$

Where $P = n$ or $1/n$ for the TE and transverse magnetic(TM) modes, respectively. The free parameters in this equation are m, $k_\perp$ and R and the p-th solution, in increasing magnitude of $k_\perp R$. The parameter p is defined as the radial mode number. We can now calculate the value for f, which is given by

$$f(m,p) = \frac{k_\perp R}{m}. \tag{2.24}$$

No analytical solution for the roots of Equation (2.23) are known and their values must either be calculated numerically or by analytical approximation. The solutions to Equation (2.23) can be substituted in Equation (2.24) for f. The total wave vector at can now be found at $R = R_0$ to be

$$k = \left[\left(\frac{fm}{R_0} \right)^2 + \left(q + \frac{1}{2} \right) \Delta E \right]^{1/2}. \tag{2.25}$$

The resonance frequency is then given by

$$\omega = \frac{c}{n}\left[\left(\frac{fm}{R_0}\right)^2 + \left(q + \frac{1}{2}\right)\Delta E\right]^{1/2}. \tag{2.26}$$

We can now describe any mode by defining the three mode numbers m, p and q and multiplying the three spacial solutions, Equations (2.13),(2.18), (2.21) and the temporal solution, Equation (2.7).

We can see from Equation (2.21) that there exists a nonzero field at the exterior of resonator. The real portion of this field are so called evanescent fields and will be discussed further in Section 2.4, and the imaginary part is propagating, representing a fundamental loss mechanism of whispering gallery modes.

2.3 Quality Factor

The Q factor is one of the most frequently used metrics to describe a cavity. Due to time and frequency's relation as canonically conjugate variables, the Q describes both the time the cavity can store energy and the bandwidth of the resonance. A large Q factor is often desirable because it can store large quantities of energy and have very narrow linewidths. In this section we define the Q factor and show how it is usually measured experimentally using the relation given by Zangwill[39, p. 702]. Then discuss the loss mechanisms that limit the Q factor in silica WGRs.

2.3.1 Energy and Linewidth

The Q is defined as

$$Q = \frac{\langle U_{EM}(\omega)\rangle}{\langle \mathcal{P}_{EM}\rangle/\omega_0}. \tag{2.27}$$

Where U_{EM} is the electromagnetic energy stored in the mode, $\mathcal{P}_{EM}$ is the energy exiting the mode per unit time, and ω_0 is the resonance angular frequency. The denominator expresses the energy lost during a 2π phase shift of the of the electric field. We start by expressing the power leaving the cavity as the time derivative of the internal energy.

$$Q\frac{\mathrm{d}\langle U_{EM}(t)\rangle}{\mathrm{d}t} = \omega_0\langle U_{EM}(t)\rangle. \tag{2.28}$$

Which is a separable first order linear differential equation. Separating the two variable and integrating gives

$$\langle U_{EM}(t)\rangle = \langle U_{EM}(0)\rangle exp\left[-\frac{\omega_0 t}{Q}\right]. \tag{2.29}$$

Since the cavity produces a phase shift, light will interfere as it circulates many times around the cavity. This means the time-average energy needs to take into account the phase. We therefore need the electric field which is proportional to the square root of the energy. Since the electric field is assumed to have a harmonic time dependence, the usual phase factor is multiplied to the expression, giving

$$E(t) = E(0)exp\left[-\frac{\omega_0 t}{2Q}\right] exp[-i\omega_0 t]. \tag{2.30}$$

We can identify $\tau = 2Q/\omega_0$ as the characteristic decay time. τ is often too short to be measured with standard photodiodes. For this reason, it is often easier to measure the Q in frequency space. Taking the Fourier transform and multiplying by the the result's complex conjugate gives the energy in the cavity as a function of the input power and laser frequency.

$$\langle U_{EM}(\omega)\rangle = \frac{U(0)}{(\omega_0-\omega)^2 + (\omega_0/2Q)^2} \tag{2.31}$$

Where ω is the laser angular frequency.This is the familiar solution to the damped driven harmonic oscillator, the Lorenzian, plotted in Figure 2.2. We can see this equation is at a maximum when the first term in the denominator is zero, $\omega_0^2 = \omega^2$, and is half the value when both terms in the denominator are equal, $|\omega_0 - \omega| = \omega_0/2Q$. Applying this calculation to both sides of the peak gives

$$|\omega_0 - \omega_{-1/2}| + |\omega_{+1/2} - \omega_0| = \frac{\omega_0}{Q}. \tag{2.32}$$

Where $\omega_{-1/2}$ and $\omega_{+1/2}$ are the frequency at half maximum on the lower and upper sides of resonance, respectively. This expression if more commonly written as

$$Q = \frac{\omega_0}{\delta\omega}. \tag{2.33}$$

Where $\delta\omega$ is the full width at half maximum in the spectrum, Figure 2.2.

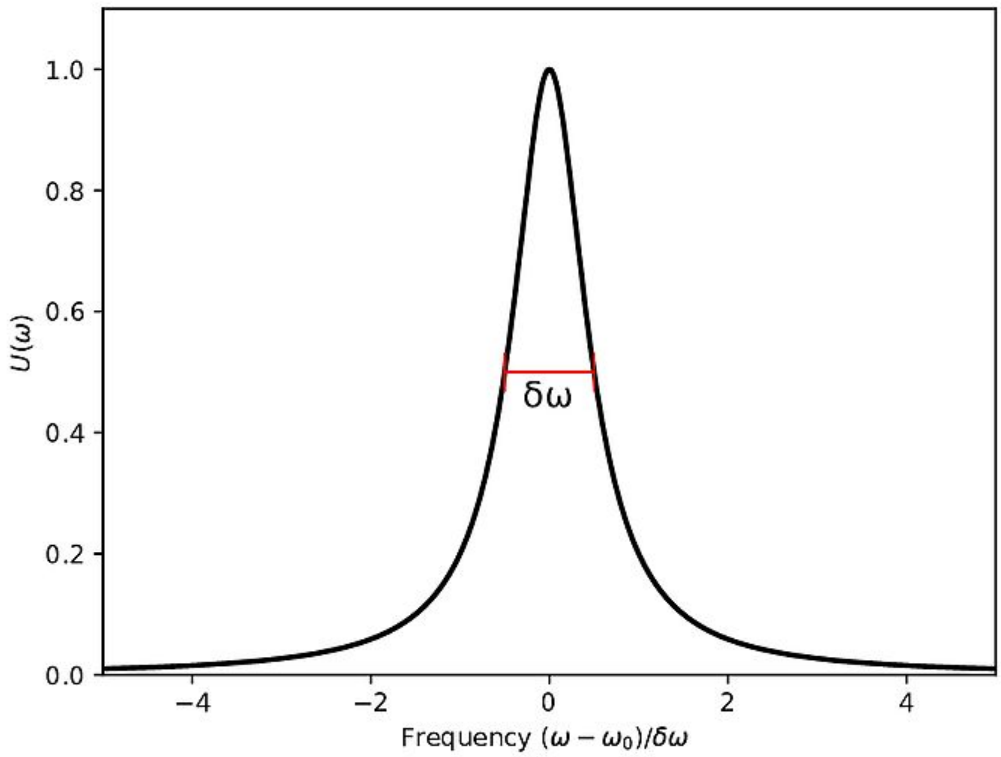

Figure 2.2: The full width half maximum of a resonance peak. Useful to measure Q factor.

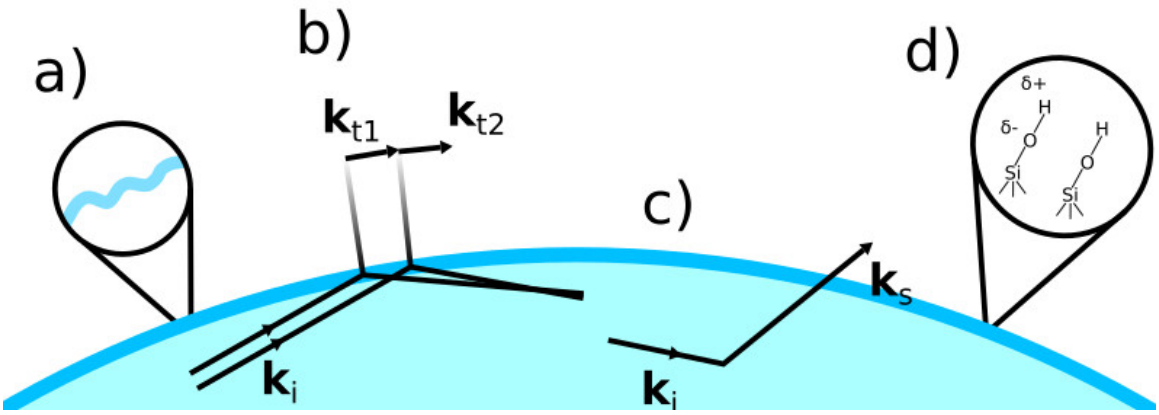

Figure 2.3: Loss mechanisms by a) capillary waves created during fabrication, b) bending loss , c) material loss (ie.: dipole radiation) , and d) chemisoption

2.3.2 Loss Mechanisms

As mentioned, Equation (2.30) indicates that the electric field in a mode behaves like a classical damped harmonic oscillator with characteristic decay time τ. The loss is in general due to a number of mechanisms and, assuming these mechanisms are all independent, τ is the sum of the inverse of the individual components.

$$\frac{1}{\tau} = \sum_i \frac{1}{\tau_i} \qquad or \qquad \frac{\omega_0}{2Q} = \sum_i \frac{\omega_0}{2Q_i}. \tag{2.34}$$

Silica WGRs have 4 types of intrinsic loss mechanisms which limit the Q[40]. These can be seen in Figure 2.3. The first is due to surface scatterers, $Q_{s.s.} \approx 10^{10}$, and is caused by capillary waves frozen into place during fabrication[40]. The second is radiation loss, $Q_{rad} \geq 10^{10}$, and is due to the curvature of the surface which couples light into free space modes[40, 41] and is expressed as the imaginary part of the solution of the radial equation, (2.21). The third is material loss, $Q_{mat} \approx 10^{10}$, which are bulk material losses. In the best cases this is mainly due to Rayleigh scattering but can also be caused by impurities and vacancies scattering[40, 42]. The fourth is contaminant scattering, $Q_{cont} \approx 10^8$, due to hydroxide groups chemically binding to the surface of the silica. These contaminant are the main source of loss and limits the Q. There are also external or coupling losses which add in the same way as (2.34) but since these losses are used as a readout they will be discussed in their own section.

2.4 Evanescent Field Coupling

In order to excite the modes and measure their response, light is coupled in and out of the WGR. The coupling methods can be categorized into 2 types[43]: free-space coupling and evanescent field coupling. Free space coupling refers to focusing a beam almost tangentially to the edge of a WGR. This is a rather inefficient method because even if the frequency matches the resonance condition, the wave vectors will differ due to the difference in refractive index, reflecting most of the light off the surface. Evanescent field coupling solves this problem by bringing a material of similar refractive index in proximity to the mode. There are a few types of evanescent field coupling methods but we only focus on tapered fiber coupling. The method requires bringing a fiber with a diameter slightly smaller than the wavelength of light near the WGR. This is currently the most efficient methods which can reach over 99% efficiency[44]. This method is also easy to set up due to the ease of manipulation of the optical fiber. In this chapter, we derive the evanescent fields and how light can couple across a section of low refractive index when incident at angles greater than the critical angle. We adapt these derivations from Cao and Yin[45]. Using this coupling method we derive the WGR transfer function and cavity field buildup factor[46]. The chapter concludes with a description of the three coupling regimes: under-coupling, critical coupling and over-coupling.

2.4.1 Evanescent Fields

Consider Maxwell's equations near a vacuum-dielectric interface where the material has refractive index n_1. The wave vector of the incident light has one component tangent and another normal to the interface, as shown in Figure 2.4. The magnitudes of fields can be expressed as

$$E = E(y)e^{i(k_x x - \omega t)} \qquad H = H(y)e^{i(k_x x - \omega t)} \tag{2.35}$$

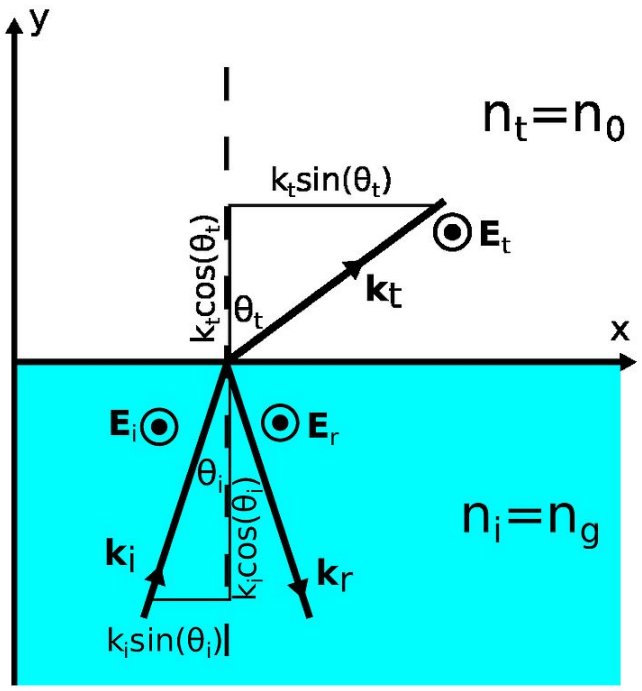

Figure 2.4: Refracting light propagating from glass to vacuum with the electric field in the z direction.

We choose the polarization of the electric field to be parallel to the interface. Using Ampere and Faraday's laws, the nonzero components are

$$k_x E_z = -\omega\mu H_y \tag{2.36}$$

$$\frac{\partial E_z}{\partial y} = -i\omega\mu H_x \tag{2.37}$$

$$ik_x H_y - \frac{\partial H_x}{\partial y} = -i\omega\epsilon E_z \tag{2.38}$$

Solving for E_z we find the Helmholtz equation.

$$\frac{\partial^2 E_z}{\partial y^2} + \left(k_0^2 n_j - k_x^2\right) E_z = 0 \tag{2.39}$$

The term in brackets is k_y, the y component of the wave vector. We can see from this equation that if $k_0^2 n_j > k_x^2$ then k_y is real[1] and the solution is a propagating sinusoidal function. In regions where $k_0^2 n_j < k_x^2$ then k_y is imaginary and the solution is exponential. Conservation of energy ensures the field will decay towards infinity,

[1]The convention is to factor in an i and call the wave vector real for propagating waves and imaginary for decaying field.

implying the light is completely reflected. The critical angle from normal incidence can be found by setting the term in the brackets equal to zero and solving to find

$$\theta_c = \arcsin \frac{n_0}{n_1} \tag{2.40}$$

as expected. From this we see that even for the case of total internal reflection, there is a non-zero electric field on the low refractive index side. A similar result can be derived for the magnetic field which, together with the electric field, forms a basis for all polarizations.

2.4.2 Frustrated Total Internal Reflection

We now add to Figure 2.4 a second section of identical dielectric placed a distance d away from the first with a plane wave moving towards the two interfaces at an incident angle greater than the critical angle as shown in the Figure 2.5a). Again, due to the continuity of the electric field parallel to the interface, k_x, will remain constant, but now, a portion of the exponentially decaying field will penetrate into the second dielectric. At that point, by Equation (2.39), the wave vector will become real again and light will propagate in the second dielectric. From this we can see that, despite total internal reflection, light can couple through a region of low refractive index even at greater incidence angle than the critical angle. This “optical tunneling", in analogy with quantum mechanics, is used to couple light in and out of WGRs, as shown in Figure 2.5 b).

2.5 Cavity Field Amplitude and Transfer Function

The amount of light which couples through the low index medium can be calculated using coupled mode theory[46]. However, coupled mode theory leads to a system of differential equations with coefficients expressed by complicated integrals for which no exact closed form analytical solution is known[46]. For this reason, we simplify the system, describing it with a scattering matrix equation and solve for the electric fields at the different ports, as shown in Figure 2.6. The cavity field buildup is the ratio at the port entering the cavity divided by the input and the transfer function is defined as the ratio of the port leaving the cavity, divided by the input field The

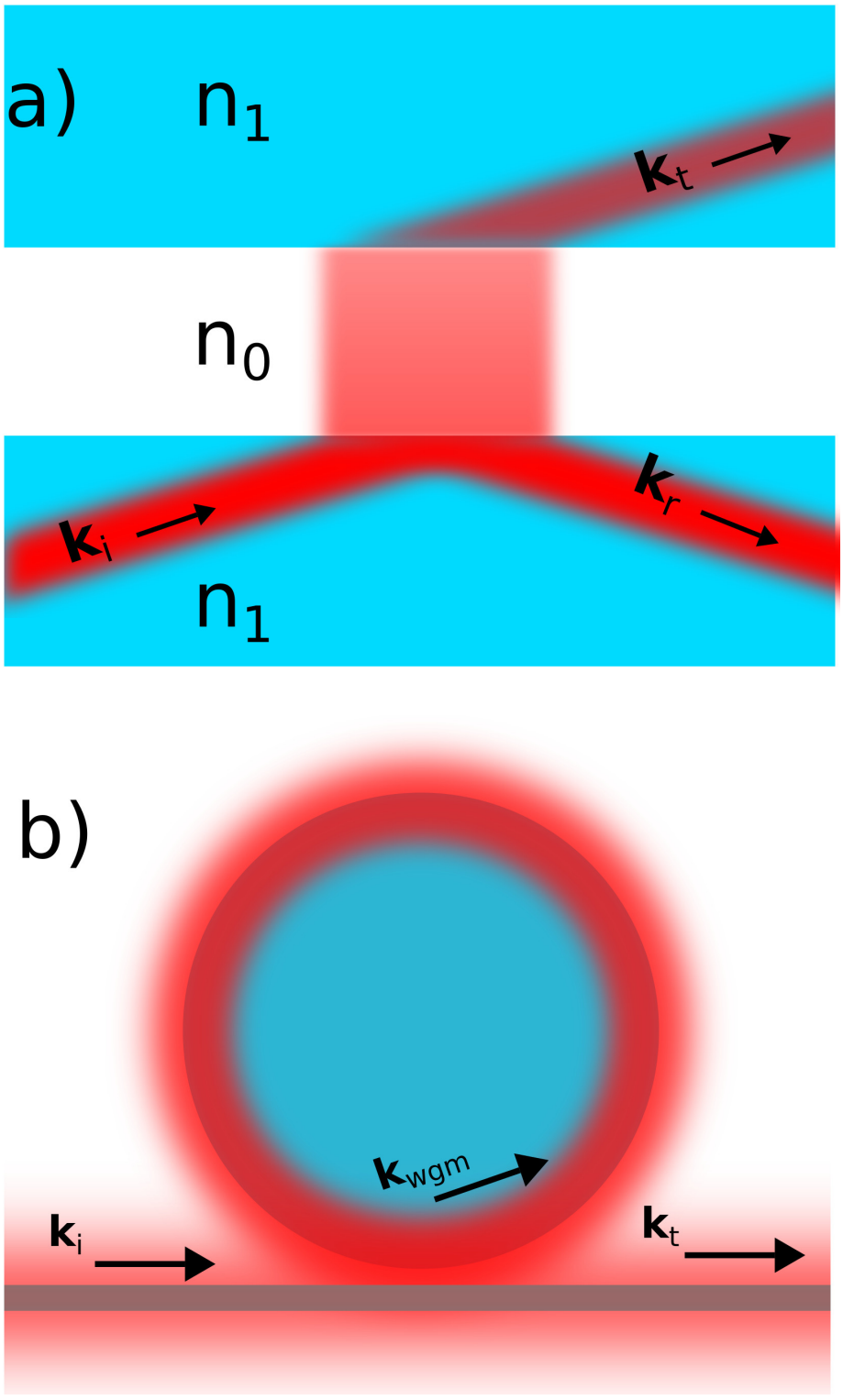

Figure 2.5: The non-zero electric field that penetrates through the region of low refractive index and into the other region of high refractive index will couple light to a propagating mode on the other side.

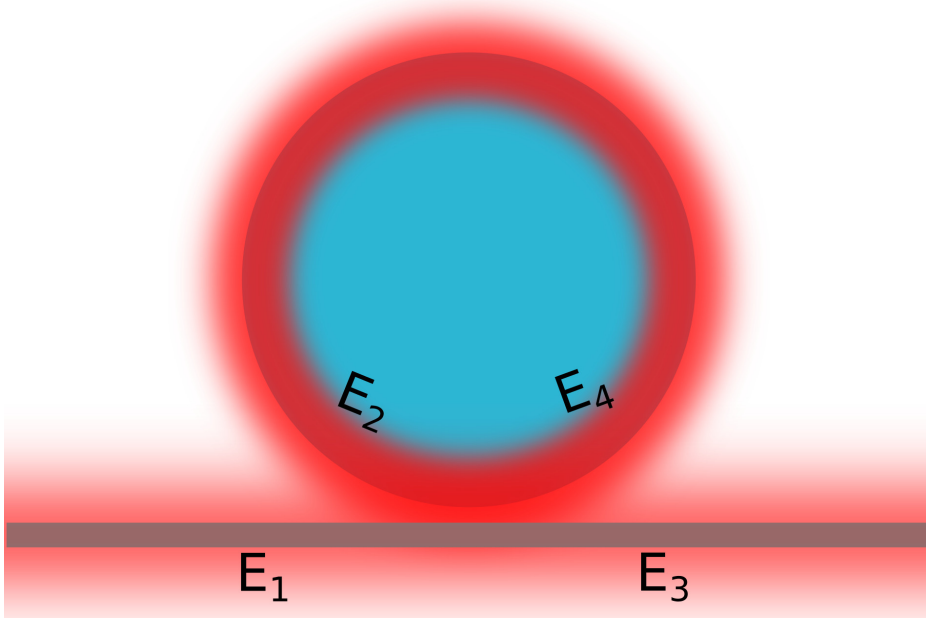

Figure 2.6: The field at all four ports, labeled 1-4, which are related through a scattering matrix equation. E_1 is the input, E_3 is the output. The light enters the cavity at E_4 and circulates towards E_2 in the counterclockwise direction.

coupling region is considered weak enough to not perturb the wave vector in either medium. The scattering matrix equation is[47]

$$\begin{bmatrix} E_3 \\ E_4 \end{bmatrix} = (1-\gamma)^{1/2} \begin{bmatrix} (1-\kappa)^{1/2} & i\kappa^{1/2} \\ i\kappa^{1/2} & (1-\kappa)^{1/2} \end{bmatrix} \begin{bmatrix} E_1 \\ E_2 \end{bmatrix} = \begin{bmatrix} S_{11} & S_{12} \\ S_{21} & S_{22} \end{bmatrix} \begin{bmatrix} E_1 \\ E_2 \end{bmatrix}. \tag{2.41}$$

Where κ is the power coupling ratio and γ is the loss due to coupling. After propagating through the cavity, the electric field E_2 and E_4 are related by

$$E_2 = E_4 e^{-\alpha L} e^{ik_{eff}L} \tag{2.42}$$

where α is the intrinsic loss of the resonator per unit length, L is the length of the mode and k_{eff} is the wave vector of the mode. The total field at ports 3 and 4 are given by the sum of the fields due to every round trip.

$$E_3 = E_1 S_{11} + E_1 S_{21}[S_{12}A + (S_{12}A)^2 + (S_{12}A)^3 + ...] \tag{2.43}$$

$$E_4 = E_1 S_{21}[1 + S_{22}A + (S_{22}A)^2 + (S_{22}A)^3 + ...] \tag{2.44}$$

Where $A = e^{-\alpha L}e^{ik_{eff}L}$ is the loss and phase factor due to the fiber during a round trip. We identify the geometric series and, after some algebra, express them as

$$\frac{E_3}{E_1} = \sqrt{\frac{1-\gamma}{1-\kappa}}e^{ik_{eff}L}\left(1-\kappa-\frac{\kappa B(e^{i\phi}-B)}{1+B^2-2B\cos(\phi)}\right) \tag{2.45}$$

$$\frac{E_4}{E_1} = \frac{\sqrt{\kappa(1-\gamma)}e^{ik_{eff}L+\pi/2}(1-Be^{-i\phi})}{1+B^2-2B\cos(\phi)} \tag{2.46}$$

Where $B^2 = (1-\gamma)(1-\kappa)s^{-2\alpha L}$ is the power lost in a round trip and $\phi = kL$ is the phase shift due to one round trip[46, 47]. Equation (2.45) is the cavity transfer function and gives the amplitude and phase response to an input electric field. The magnitude squared is proportional to the power which is typically the measured quantity at the detector. The phase information is usually lost because the photodectors don't have the bandwidth to respond to infrared frequencies. Certain experiments, however, involving heterodyne or lock-in detection do allow us to measure the phase information as we shall see in chapter 5. Equation (2.46) gives the field at port 4, and approximately the whole cavity.

2.6 Coupling Regimes

As mentioned in Section 2.3.2, the process of coupling light out of a WGR constitutes an external loss mechanism which decreases the Q and can be characterized by the decay time τ_{coup}. This loss mechanism can be tuned by adjusting the tapered fiber's radius and distance from the WGR. Mathematically, these parameters change κ and the couple is classified into three regimes: undercoupling, critical coupling and overcoupling.

- When the coupling is weak $\kappa < 1-(1-\gamma)e^{-2\alpha L}$ the system is said to be **undercoupled**. We can see from the transfer function that in this regime, when on resonance $\phi = 2\pi m$ for some integer m some light will always reach the detector. This portion of light effectively does not enter the cavity.

- When $\kappa = 1-(1-\gamma)e^{-2\alpha L}$ the system is said to be **critically coupled**. This condition occurs when the cavity's intrinsic decay time τint is equal to the coupling decay time τ_{coup}. This is easily recognizable by the transfer function being equal to zero on resonance. At this frequency all the light enters the

cavity and all the light is lost by the mechanisms discussed in 2.3.2. It may seem odd that none of the light is lost due to coupling out of the resonator, however this is due to $\pi/2$ phase shifts experienced during frustrated total internal reflection[46] which cause destructive interference at port 3. These phase shifts appear in the off diagonal terms of the scattering matrix (2.41)[46]. At this coupling, the fields inside the cavity are at their maxima, and is desirable for most applications requiring large power.

- When $\kappa > 1-(1-\gamma)e^{-2\alpha L}$ the system is said to be **overcoupled** and a portion of the light coupled in will be coupled out before being lost by the intrinsic loss mechanisms. In this regime a portion of light will always reach the detector.

Chapter 3

Measurement of SNAP Radius Profile and Mode Refractive Index

This chapter presents a technique which, assuming separation of variables is valid, can measure the refractive index and absolute radius of a SNAP. This work improves work done by Sumetsky and Dulashko[48], and Birks et al.[49] who measured the radius variation given the refractive index. The improvements are that we measured the absolute radius and not radius variation. We also drop the assumption that the modes are near the interface, which is equivalent to setting $f = 1$. Furthermore, these papers do not have an accurate way of differentiating between variations in radius and variation in refractive index. This differentiation is particularly useful because it would provide a way to measure two physical phenomena simultaneously with one resonator(i.e.: temperature and pressure). Besides the application to sensing, this would also provide a platform to study the physics and chemistry of surfaces, since the radius could be determined to the accuracy of the standard deviation of the surface roughness.

In this experiment, the procedure was attempted on a SNAP, for which separation of variables is only valid for the first few significant figure but, at very high precision, the coupling between the two directions is too large to ignore. This means we could not obtain accurate values beyond the precision in which separation of variables is valid. For this method to work, we would either need a WGR with a smaller radius variation, or a better theoretical model that can more accurately account for the radius variations.

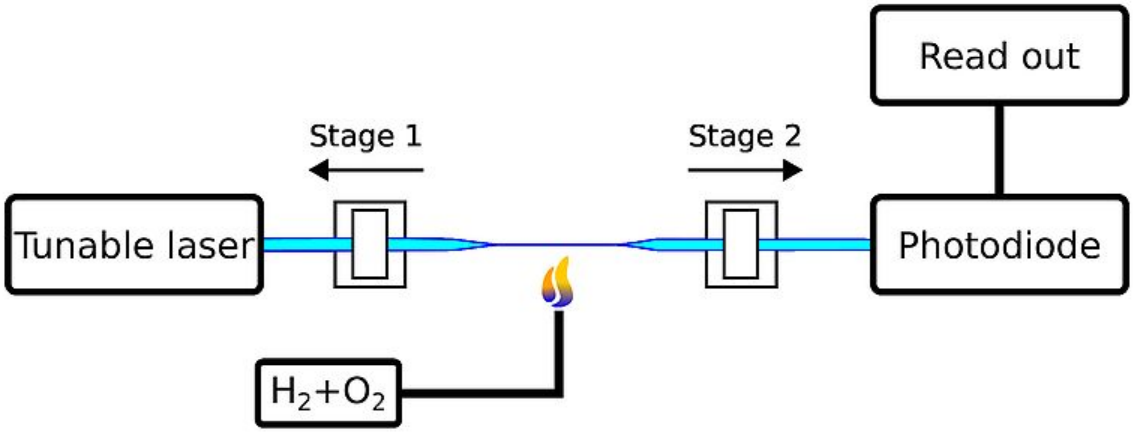

Figure 3.1: The tapered fiber and SNAP fabrication setup. As the flame heats the fiber, the two stages pull the fiber apart while moving it back and forth to heat the entire region being pulled. The tunable laser, photodiode and readout are only used for the fabrication of the tapered fiber.

We start this chapter by describing the fabrication and the experimental setup and present the data. Once the data is properly visualized, the theory of the analysis is presented. Then these methods are applied to the data, and the final result is presented.

3.1 Fabrication

Both the tapered fiber and SNAP are fabricated by elongating a single mode optical fiber, using the flame brush technique described by Bilodeau et al.[50] and Birks[51]. The fiber is first stripped of its protective jacket and cleaned with isopropanol, leaving the cladding exposed. The fiber is then clamped to two linear stages as seen in Figure 3.1. While being heated with a hydrogen-oxygen torch, the stages pull the fiber while sweeping over the flame.

3.1.1 Fabrication of a Tapered Fiber

The shape of the tapered fiber is cylindrically symmetric with a double exponential radius profile as described in [51]. When fabricating the tapered fiber, a laser, photo detector and readout are used to monitor the transmission as shown in Figure 3.1. During the pulling process, the diameters of the core and cladding are both reduced.

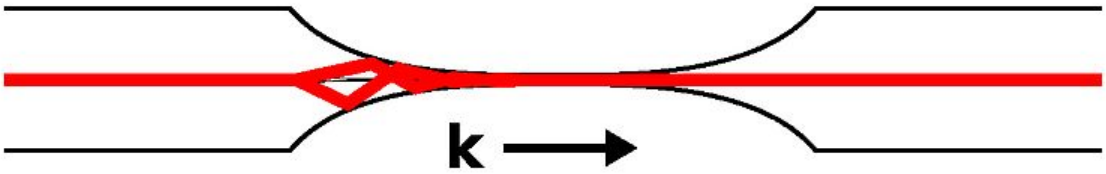

Figure 3.2: A depiction of light traveling through a tapered fiber from left to right. The light starts in the core's single mode, once the core is too small to support the mode the cladding will guide multiple modes until all the mode are funneled into a single mode with an evanescent field outside the fiber.

The core is eventually reduced beyond the diffraction limit and the light is only guided by the cladding. The light leaks out of the core and is strongly guided by the cladding in multiple modes which interfere at the detector. As the fiber is reducing, the interference changes producing oscillations in the transmission readout. The fiber is further pulled until all the modes converge to the fundamental mode. This is identified when the transmission ceases to vary and occured when the narrowest part of the fiber is approximately 1 μm. This strongly guided single mode now has a an evanescent field, which is accessible for coupling into the SNAP. Figure 3.2 depicts the end result where we can spatially see all three regions described in the pulling process. It is worth nothing that the evanescent fields increase with decreasing radius[52]. We can use this to tune the coupling regime by moving the SNAP to parts of the taper with different radii.

The tapered fibers are fragile and must be epoxied to a mount before the clamps are removed as shown in Figure 3.2.

3.1.2 Fabrication of a SNAP

SNAPs are fabricated using the flame brush technique developed by Hamidfar[53]. Manufactures fabricate optical fiber such that the radius variations are too small to stably confine a modes in 3 dimensions. This means only one mode can be supported, where there is no propagation along the fiber. To create the radius variations for a SNAP we us the same setup as the tapered fiber minus the laser, detector and readout. The non-uniformity of our pulling system creates variation in the radius that are large enough to confine the light along the axis as shown in Figures 2.1 and 3.3.

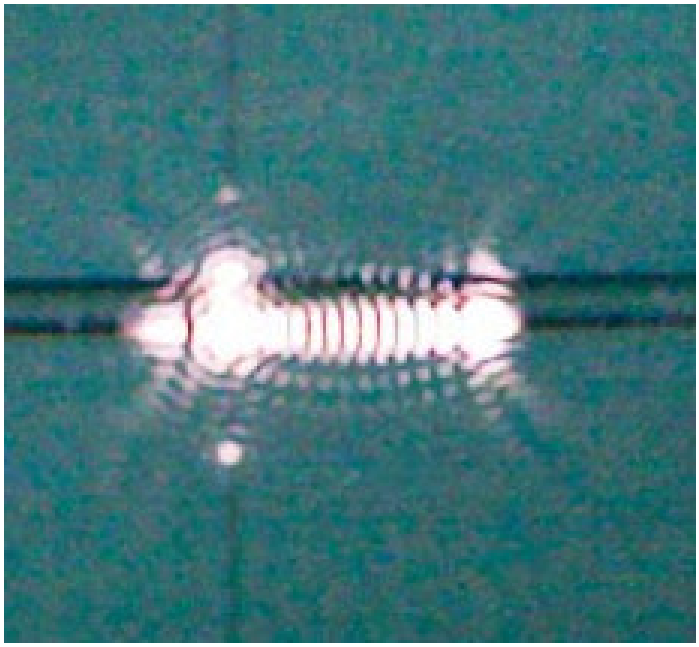

Figure 3.3: Picture of a SNAP with an excited mode[54] producing a standing wave pattern along the axis.

3.2 Experimental Setup

We wish to plot a spectrogram to visualize the transmission as a function of position along the fiber, and laser wavelength. To collect this data, we need a series of spectra along the SNAP at a high enough resolution to see the standing wave pattern along the axis. A schematic of the setup can be seen in Figure 3.4 and the list of equipment used in Table 3.1. To collect a single spectrum, a tunable laser scans over a range of wavelength, sending a small portion of the light to a wavelength locker with known resonance frequencies. The electronic outputs of the wavelength locker are then sent to the oscilloscope. This acts as a ruler in frequency space for which all frequencies between resonances can be interpolated during the laser's scan. Most of the light is sent to the SNAP, where it is coupled in and out as described by the transfer function, Equation (2.45). The power of the transmitted light will be detected at the photodiode and shown on the oscilloscope. The direct connection from the laser to the oscilloscope is the trigger which signal the start of the scan.

After collecting one spectrum, a micro-motion controller moves the SNAP along its axis by 1 micron and collects the next spectrum, repeating these steps for 1000 spectra. Thus acquiring spectra along a 1mm length of the fiber containing the SNAP.

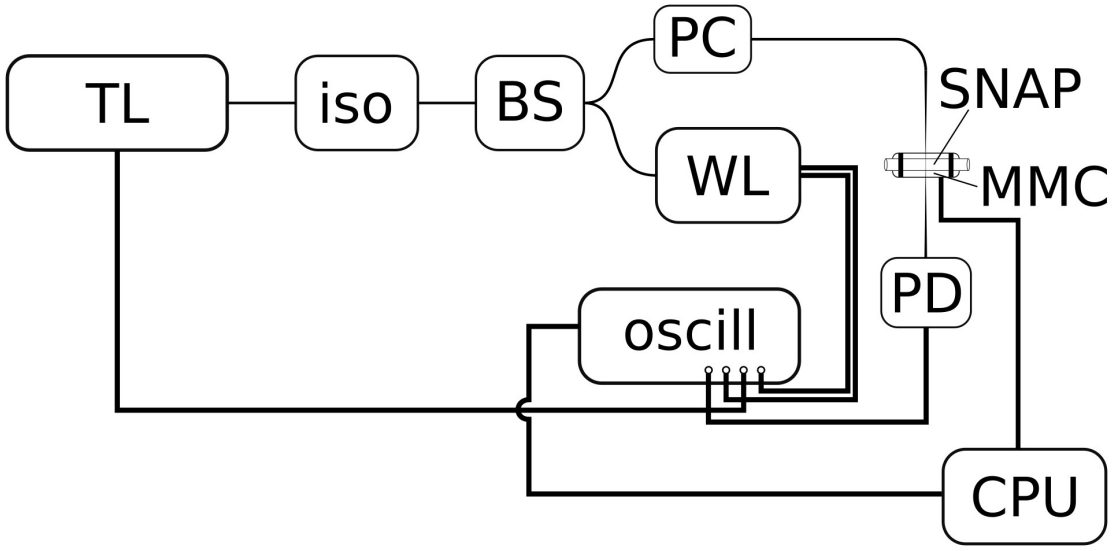

Figure 3.4: Schematic of the experimental setup. TL: tunable laser, iso: isolator, BS: 90/10 beam splitter, PC: polarization controller, SNAP: resonator, MMC: micro motion controller, PD: photo detector, oscill: oscilloscope, WL: wavelength locker, CPU: computer. Optical fibers are represented by thin lines and electrical wires by thick lines.

Component	Manufacturer	Model
Tunable laser	GN-Nettest	TUNICS-plus 3644HE-15
Isolator	E-TEK	IW DM A410CRV 06
Beam splitter	Fiber Optics Communications Inc.	C-WS-AL-05-S-1210-15-AP/AP
Wavelength locker	JDS Uniphase	FPWL 211501100
Polarization controller	OZ Optics	FPC-100
Micro motion controller	Micronix USA	PPS-20 (x3)
Photo detector	Thorlabs	PDA 10CF
Oscilloscope	Tektronix	MDO 4034

Table 3.1: List of components used in experimental setup (Figure 3.4).

This is coordinated using an in house Python script written by Matias Rittatore, Pablo Bianucci, and the author. While the laser repeatedly scans over the wavelength range, the program signals the oscilloscope to acquire a single spectrum upon the next trigger. Once triggered, the oscilloscope starts collecting data, sending it to the program which saves it to a file. The program then moves the SNAP to the next position and restarts the loop by signaling the oscilloscope to acquire the next spectrum.

3.2.1 Spectrum Calibration and Spectrogram

The raw data consists of 4 channels: transmission, wavelength locker Fabry-Perot, Trigger and Wavelength locker power monitor. An example of the raw transmission data and the wavelength locker data is plotted in Figure 3.5a) and b) respectively. To convert this data to transmission as a function of wavelength, a calibration script was written in R programming language by the author, then implemented in Python by Pablo Bianucci.

The wavelength locker is calibrated such that the known frequencies are where the Fabry-Perot and power monitor cross with an downwards slope, when plotted for scans of increasing wavelength. These points are marked by red lines in Figure 3.5 b). The trigger's low and high values are dependent on the scanning range. The script uses this to identify the starting wavelength. All the points between the wavelength locker's known frequencies are linearly interpolated.

The laser and optical circuit has many frequency dependent losses which results in power oscillations in the transmission. To separate these effects from the effects of the SNAP and to convert the photo detector output to a normalized transmission, every spectrum's transmission is normalized by the transmission of a scan without a SNAP. A spectrum after wavelength and power calibration is shown in Figure 3.5 c).

Separate Python and R scripts were written by Pablo Bianucci and the author to take all the calibrated spectra, at each position along the SNAP, and plot the transmission as function of wavelength and position. The resulting spectrogram can be seen in Figure 3.6.

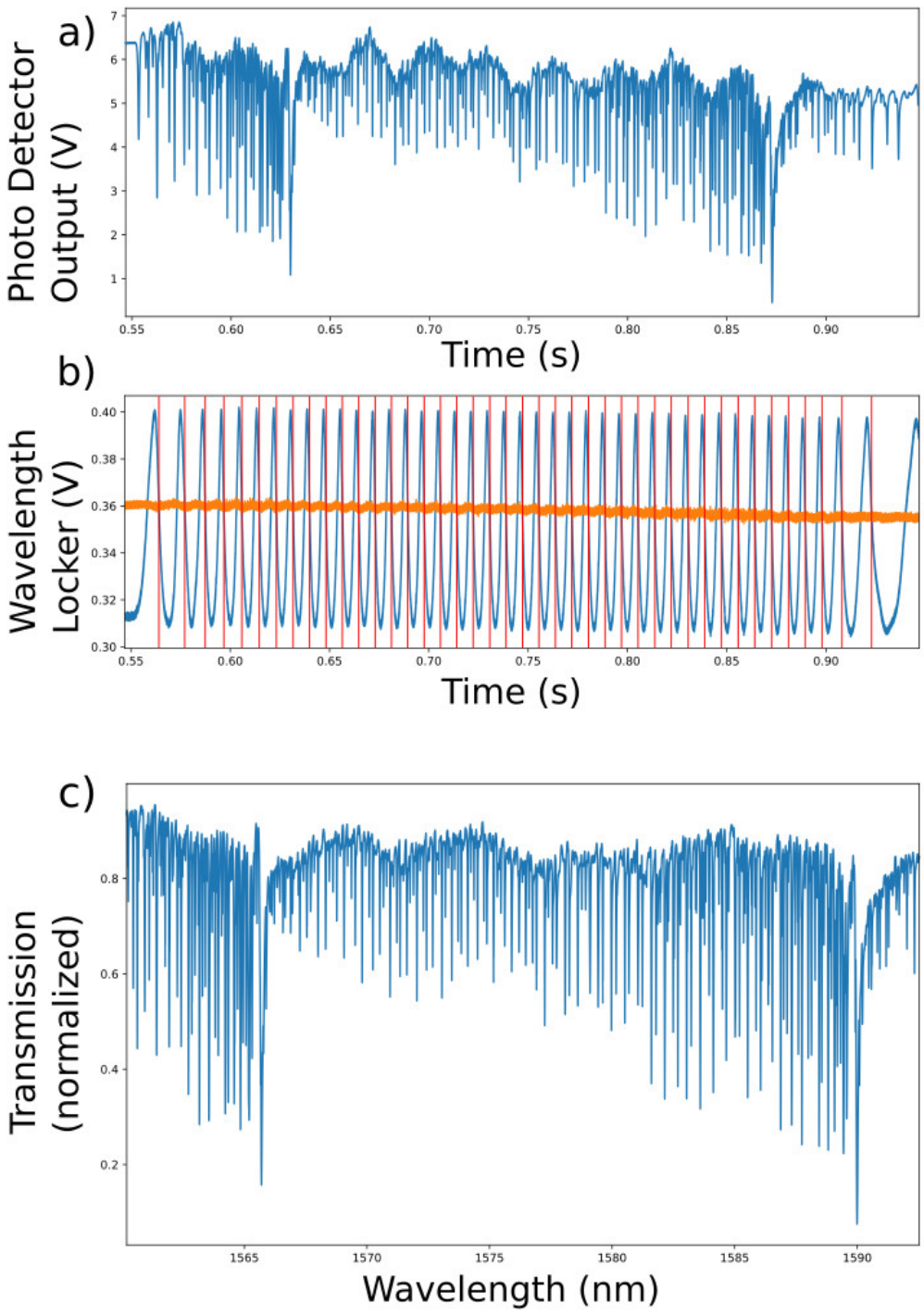

Figure 3.5: Conversion of raw data from time domain to wavelength domain. a) Transmission as a function of time during scan. b) Wavelength locker data, the known wavelengths are where the Fabry-Perot(blue) crosses the monitor(orange) indicated by the vertical read lines. c) Data after power and wavelength calibration.

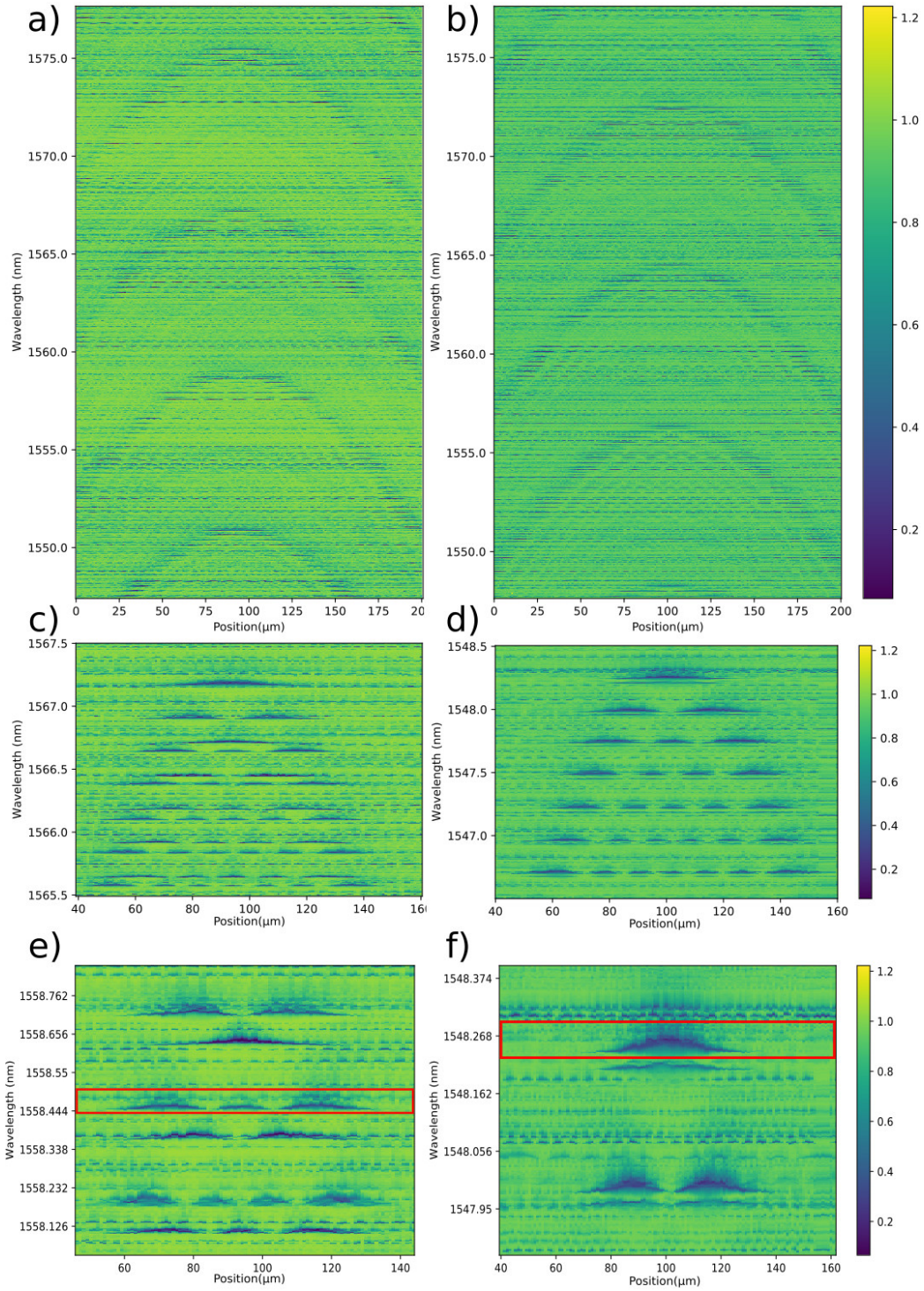

Figure 3.6: Spectrogram of transmission as a function of wavelength and position along the SNAP's axis. a) and b) are spectrogram showing multiple azimuthal mode numbers of orthogonal polarizations, respectively. c) and b) are enlarged portions of a) and b), respectively. We can see two of sets of modes, the strongly coupled modes are the 1st order radial modes and the weaker coupled modes are the 2nd order ones. e) and f) are the enlarged sections of c) and d). The red boxes indicated the rows that were averaged when finding the turning points.

3.3 Theory

Simply put, we pick a large set of modes that correspond to the same axial mode number and adjust the parameters in the TEq until all the modes are consistent with one value for the radius and refractive index.

The value of the radius will be determined at the turning points because, at these points, the wave vector is completely in the azimuthal direction. We can therefore set $k_\perp = k$, dropping the subscript.

From the spectrogram, we can make the following assumptions about the set of modes with a given axial mode number:

- The radial mode number can be determined by the coupling strength. The more strongly coupled modes are the 1st order and the more weakly coupled modes are the 2nd order radial modes.
- Consecutive modes with the same radial mode number differ only by 1 azimuthal mode number.
- The modes have a common turning point and common radius at the turning points.
- The initial, approximate, refractive index is good enough to calculate the mode numbers and polarization.

From these, we will show that the azimuthal mode numbers and polarizations can be determined. Once these are found, the refractive index can be varied such that all the modes give the same value for the radius.

This section is divided into 3 parts. First, the method to determine turning points along the fiber is presented. Then, the method for determining the mode numbers and polarization is derived. Finally, the improved error is derived when the refractive index is varied to minimized the difference between the model and the data of the two modes of orthogonal polarizations.

3.3.1 Location of the Turning Points

The turning points are the two points along the axis where there is no propagation along the axis and therefore $k_z = 0$. By setting this value in the differential equation

for the axial direction, Equation (2.16), we find

$$\frac{\partial^2 Z(z)}{\partial z^2} = 0. \tag{3.1}$$

Since the second derivative is also zero where the $Z(z) = 0$, we must specify that only the zeros at the far edges of the mode are of interest. This is indicated by the red lines in Figure 3.7, where the field amplitude, and its second derivative are plotted. We now need to obtain a similar plot from the data. In the spectrogram, Figure 3.6 e) and f), we can select a subset of rows, like the ones boxed in red, that couple into a single mode. These rows can be averaged over to obtain the transmission at every position. From this, we can plot the stored energy in the resonator as function of position. By Poynting's theorem, the square root of this yields a function proportional to the absolute value of the fields. Taking the second derivative of this new function and finding the roots on either edge will give us the turning points.

3.3.2 Determining Mode Numbers and Polarization

For large azimuthal mode numbers, the free spectral range is approximately, but not exactly, equal for consecutive modes. This small difference can be used to determine the azimuthal mode numbers. We do this by finding the roots of the TEq, Equation (2.23), for two modes numbers that differ by a known number of azimuthal mode numbers q and dividing them.

$$\frac{k_m R}{k_{m+q} R} = \frac{\lambda_{m+q}}{\lambda_m}. \tag{3.2}$$

This value can be measured as it is the ratio of two resonance wavelengths, with identical axial mode number and known difference in azimuthal mode number. This ratio is monotonic with increasing m, allowing us to try different values for m until the theoretical and the experimental values are consistent.

3.3.3 Determining the Refractive Index and Radius

To visualize how the refractive index is determined, Figure 3.8 shows a plot of the TEq for two axial modes, for a theoretical SNAP of $40\mu m$. The TEq's were plotted as a function of radius instead of the product kR. This was done by calculating the TEq for correct mode numbers and multiplying by $\lambda_{res}/2\pi$. Figure 3.8 b) and c)

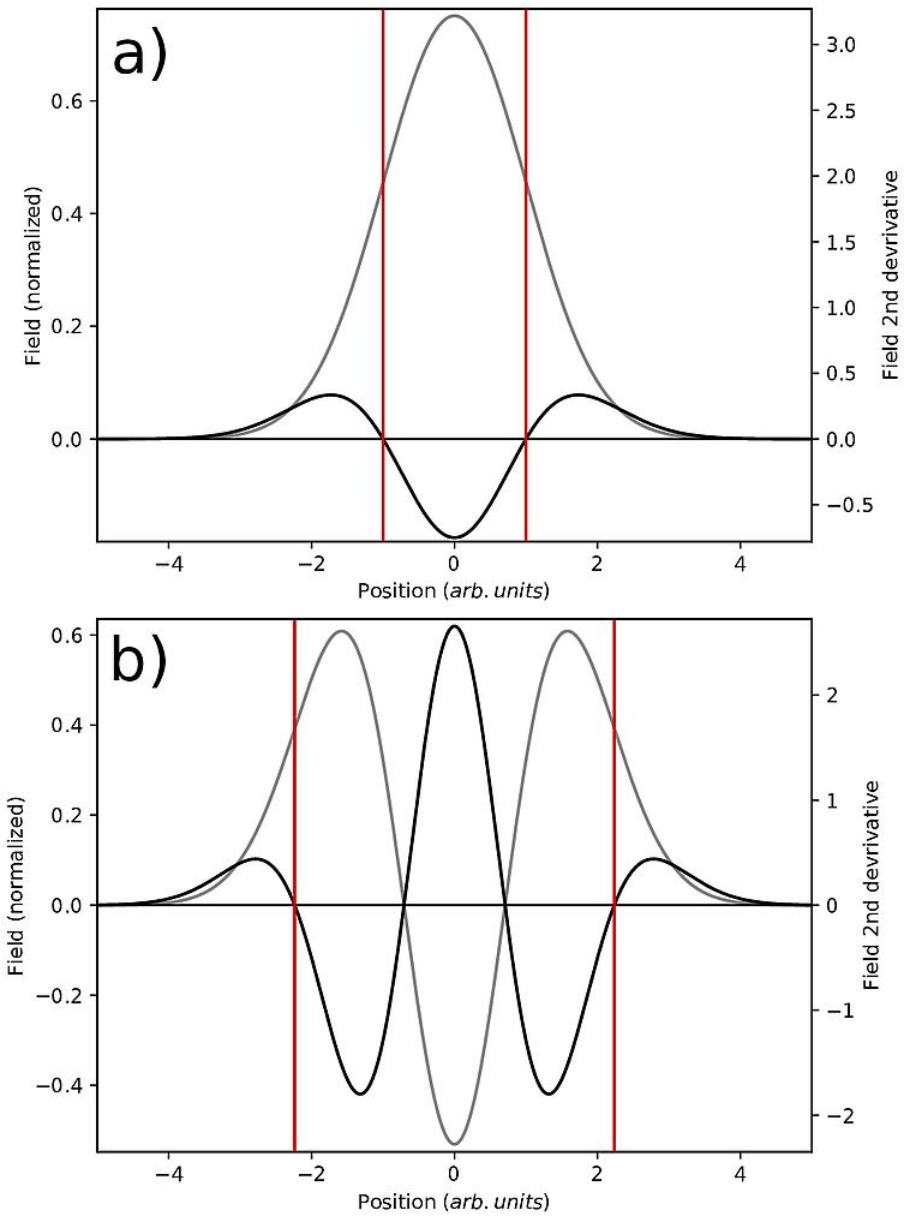

Figure 3.7: Field(gray) due to an effective harmonic potential along the axis and its second derivative(black). a) First axial mode and b) third axial mode. The turning points are marked by red lines.

focuses on the first zero, which corresponds to the radial mode number of interest for this theoretical SNAP. In b), the refractive index is the correct value, confirmed by the fact that both TEq's correspond to the same radius. If the refractive index is varied, we can see from c) that the TEq's have different zeros, corresponding to different values of the radius at the position of the turning point. This is a physically impossible scenario. In our experiment, the value of n will start off as having some error which will be varied such that the two modes coincide.

The initial error is given as a function of the two continuous parameters in the TEq: the wavelength and the refractive index,

$$\delta R = \frac{\partial R}{\partial \lambda_{res}} \delta\lambda + \frac{\partial R}{\partial n} \delta n \tag{3.3}$$

Where δR is the error in the measured radius of the modes, λ_{res} is the free space resonance wavelength, $\delta\lambda$ is the error in the measured resonance wavelength and δn is the error in the refractive index.

The manufacturer of the wavelength locker guaranties the measurement to within 20 pm, and since this error is larger than the 1 pm random noise observed in the data, this is a bias. The initial, approximate refractive index will also bias our values, which means the difference in measured radius is just the difference in their errors.

$$R_1 - R_2 = \delta R_1 - \delta R_2 = \left(\frac{\partial R_1}{\partial \lambda_{res}} - \frac{\partial R_2}{\partial \lambda_{res}} \right) \delta\lambda + \left(\frac{\partial R_1}{\partial n} - \frac{\partial R_2}{\partial n} \right) \delta n, \tag{3.4}$$

where the subscripts identify the mode.

By the assumption that the exact radius is common for both modes, the approximate refractive index can be varied such that the left hand side is zero. This can be seen from Figure 3.8 B) and C) where the difference in measured radius is zero when correct refractive index is used. In the correct refractive index, Equation (3.4) reduces to

$$\delta n' = \left(\frac{\partial R_2}{\partial n} - \frac{\partial R_1}{\partial n} \right)^{-1} \left(\frac{\partial R_1}{\partial \lambda_{res}} - \frac{\partial R_2}{\partial \lambda_{res}} \right) \delta\lambda, \tag{3.5}$$

where $\delta n'$ is the error of the improved refractive index, after varying. The new value of the refractive index can then be used to calculate the radius, and the new error can be substituted back into Equation (3.3) to obtain the improved error in the radius. To minimize δn, the modes need to be chosen such that the coefficient of $\delta\lambda$ in Equation (3.5) is small. By choosing modes of orthogonal polarization, the different

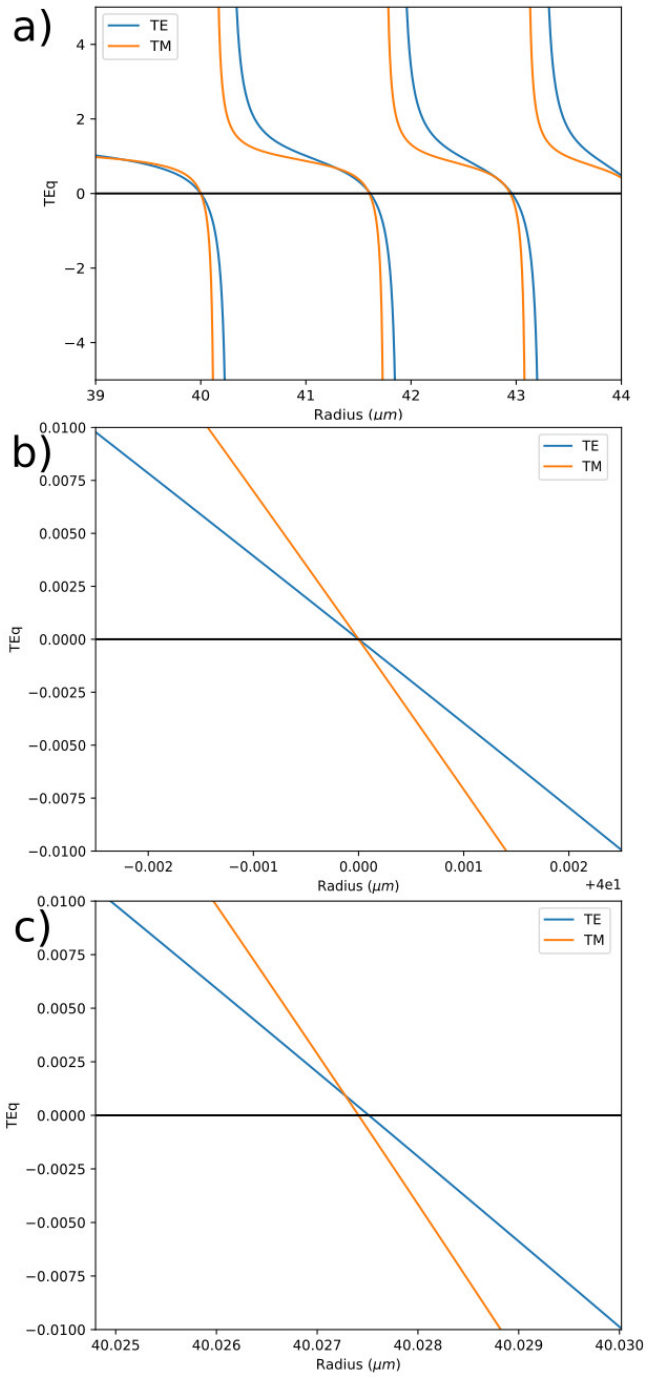

Figure 3.8: The TEq for a TE and a TM mode as a function of radius. The theoretical resonator has a radius of 40 μm. b) is an enlargement on the first zero in a) where the refractive index was the correct value of 1.445. In c) the TEq was calculated with a varied refractive index of 1.444. It can be identified as wrong by the fact that the modes indicate a different radius.

dependencies of the TEq on the refractive index will lead to a large difference in the coefficients of n in Equation (3.3) when compared to mode of same polarization. For this reason, use of orthogonal polarizations is favorable, giving

$$\delta n' = \left(\frac{\partial R_{TM}}{\partial n} - \frac{\partial R_{TE}}{\partial n}\right)^{-1} \left(\frac{\partial R_{TE}}{\partial \lambda_{res}} - \frac{\partial R_{TM}}{\partial \lambda_{res}}\right) \delta\lambda. \tag{3.6}$$

3.4 Analysis and Results

We are now in a position to measure the refractive index and radius. In this section we apply the methods of the previous section to the first and third axial modes in the spectrogram, Figure 3.6 e) and f), boxed in red.

3.4.1 Determining the Turning Points

We select axial modes 1 and 3, boxed in red in Figure 3.6 e) and f). The average transmission for every position was computed. Figure 3.9 a) and b) shows this averaged transmission, subtracted and normalized to obtain the power, as a function of position, lost in the cavity. A $6\mu m$ moving average filter was used to remove high spatial frequency noise. A square root was applied to obtain a function proportional to the absolute value of the electric field. The second derivative of this was computed using a second order accurate central differences, then plotted in Figure 3.9 c) and d). The turning points are marked by red lines.

3.4.2 Determining the Mode Numbers and Polarizations

The mode numbers were determined by comparing the theoretical and measured values from Equation (3.2) and picking the best fit. Figure 3.10 shows the plot of the theoretical wavelength ratio for modes that are 8 mode numbers apart. The blue dots correspond to the TM modes and the orange dots to the TE modes. The red line indicates the experimental value of quotient of two modes separated by 8 axial mode numbers. The correct value correspond with the dot that coincides with the red line. The only combination of mode numbers that was possible is shown in Table 3.3. Some comparisons of theoretical and measured values are shown in Table 3.2.

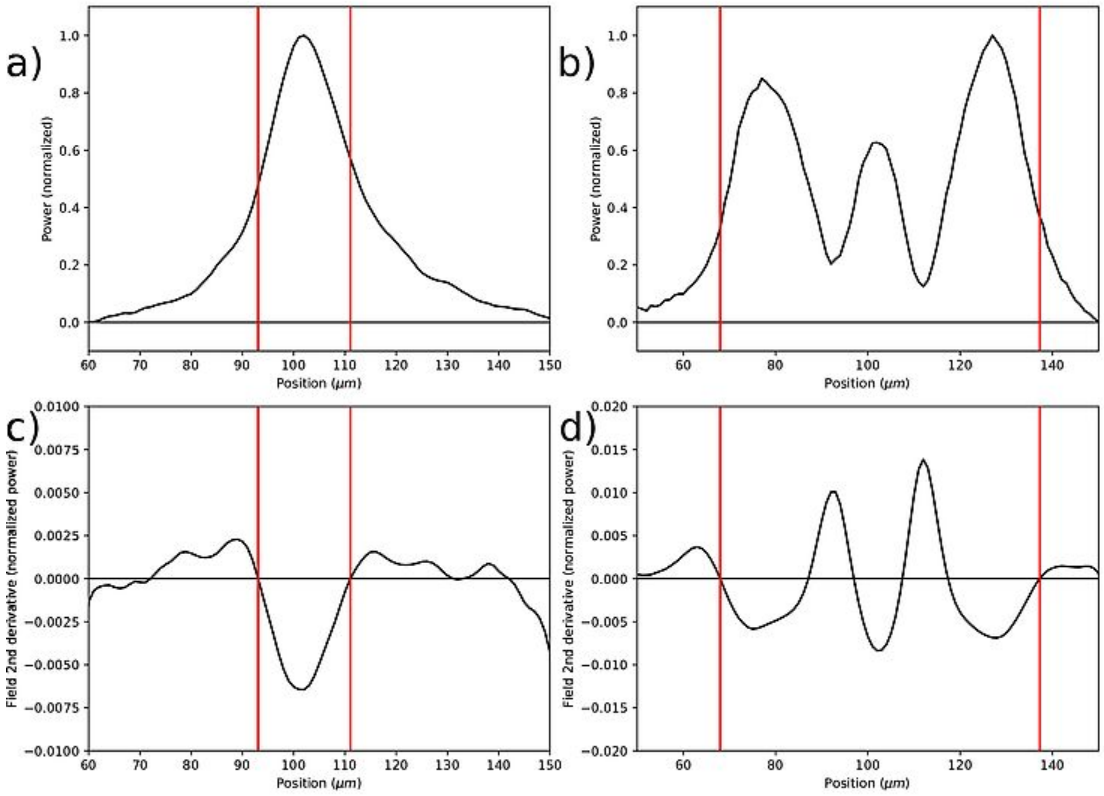

Figure 3.9: a) and b):Power lost in axial modes 1 and 3. c) and d): Second derivative of the square root of the a) and b), respectively. The turning points are marked by red lines.

Theoretical λ_1/λ_2	Measured λ_1/λ_2	Error($\times 10^{-5}$)	m_1	m_2	p	Polarization
1.037145	1.037155	1.0	182	189	0	TM
1.032146	1.032172	2.6	175	181	1	TM
1.015561	1.015552	-0.9	187	190	0	TE
1.043246	1.043211	-3.6	174	182	1	TE

Table 3.2: Comparison of theoretical and measured values of the ratio of pairs of wavelength for the first axial mode number. These values show both polarizations, where both the first and second radial mode numbers must be within the allowed error.

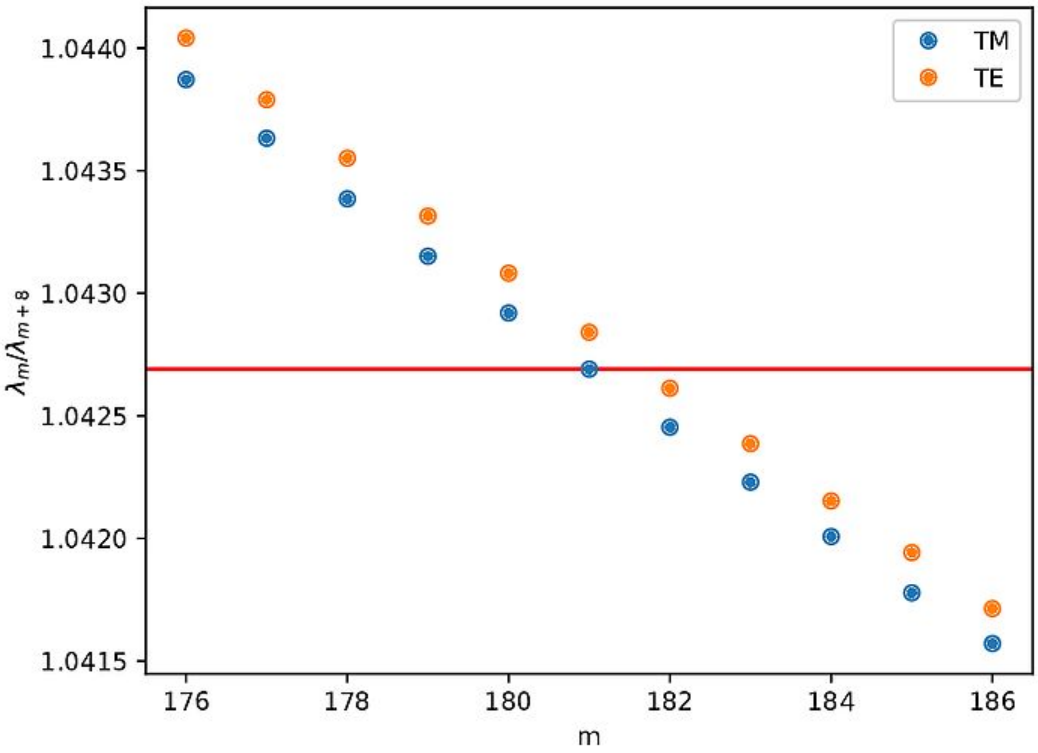

Figure 3.10: Ratio of resonance wavelengths for modes separated by 8 azimuthal mode numbers as a function of the smaller mode number. The red line is the experimental value and the error is $\pm 10^{-5}$. The correct data point is where the dot coincides with the line.

λ(nm)	m	p	Polarization	λ(nm)	m	p	Polarization
1548.237	189	0	TM	1542.710	190	0	TE
1556.186	188	0	TM	1550.635	189	0	TE
1564.239	187	0	TM	1558.624	188	0	TE
1572.369	186	0	TM	1566.702	187	0	TE
1580.586	185	0	TM	1574.861	186	0	TE
1588.892	184	0	TM	1583.107	185	0	TE
1597.282	183	0	TM	1591.439	184	0	TE
1605.761	182	0	TM	1599.858	183	0	TE
1614.333	181	0	TM	1608.369	182	0	TE
1548.205	181	1	TM	1542.818	182	1	TE
1556.302	180	1	TM	1550.855	181	1	TE
1564.466	179	1	TM	1558.965	180	1	TE
1572.722	178	1	TM	1567.165	179	1	TE
1581.063	177	1	TM	1575.448	178	1	TE
1589.500	176	1	TM	1583.821	177	1	TE
1598.014	175	1	TM	1592.283	176	1	TE
1606.628	174	1	TM	1600.839	175	1	TE
1615.333	173	1	TM	1609.484	174	1	TE

Table 3.3: Mode numbers computed using Equation (3.2) for all the first axial mode number.

Polarization	Axial Number	R(μm)	ΔR(nm)	Left TP(μm)	Right TP(μm)
TM	1	33.554	1.9	95	110
TM	3	33.543	2.0	70	135
TE	1	33.489	5.5	95	110
TE	3	33.478	5.8	70	135

Table 3.4: Average radius of all the modes with the given polarization and axial mode number. ΔR is the standard error of measured radius. The two last columns are the location of the turning points.

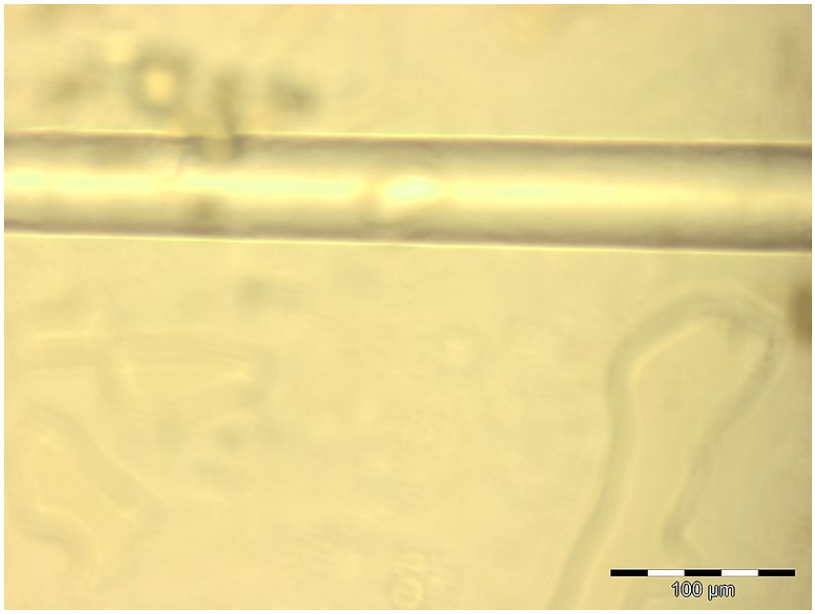

Figure 3.11: Picture of a SNAP from an optical microscope shows a diameter of about $65\mu m$.

3.4.3 Radius Measurement

The radius was calculated by multiplying the root of the TEq by $\lambda_{res}/2\pi$ for the corresponding mode numbers and polarization. The initial refractive index was estimated using the manufacturer's specification for the core refractive index and the numerical aperture. The value was $n = 1.462$. The results are shown in Table 3.4 and are consistent with measurements from an optical microscope of a $65\mu m$ diameter shown in Figure 3.11

We see a discrepancy for the measured radius given by each polarization. If separation of variables were valid, the refractive index would be varied until both values matched. In our case, the variation is too large, and this procedure gives

a value well below 1.4, which cannot be correct. To estimate the limit for which separation of variable is valid, we calculate the ratio [36] using a linear approximation between the two calculated radii at the two turning points.

$$\frac{k_r}{k_z} = \frac{\mathrm{d}R}{\mathrm{d}z} \approx 1.5 \times 10^{-3}, \tag{3.7}$$

where the profile was assumed to be parabolic. This is consistent with the discrepancy of the two polarizations. Multiplying the radius by this value gives an estimate of the precision in the model of the model.

$$33.5 \times 10^{-6} m \times 1.5 \times 10^{-3} = 50\ nm \tag{3.8}$$

Since this correspond to a radius of $33.5 \pm 0.05\ \mu m$, we cannot improve our measurement of the refractive index, or of the radius, using this theoretical model.

This error in the model must be added to Equation (3.3) using our estimate refractive index. The error in the model will be the largest contributor, giving a total error of 69 nm.

3.5 Discussion and Outlook

The radius variation of the SNAP was too large to use this technique with the given model. A more accurate model is needed to take into account the fact that the modes have a non-negligible radial component. Alternative, a SNAP with a smaller radius variation, such that the ratio of the components of the wave vectors in the radial and axial directions, Equation (3.7), is less than 10^{-6}. This would give 6 significant figures, enough to have have 0.1 nm precision with a radius on the order of 10 μm.

Regardless of the failure to measure the absolute radius and refractive index, we were able to accurately determine the mode's azimuthal number, radial numbers, polarization and the turning points using only the spectrogram while not relying on the approximation of the light being near the interface.

Chapter 4

Nanoparticle Carousel Induced Periodic Resonance Shift

Nanoparticle trapping was largely pioneered by Ashkin et al. in 1970s and 1980s [55–57], where particles, suspended in water, were trapped by a laser beam or a combination of a laser beam and gravity. These effect were much later studied in WGRs by Arnold et al. [9], where nanoparticles were trapped in the evanescent field of a microsphere. These trapped particles also experience a scattering force which propels the nanoparticle in the direction of the propagating light. The previous year, Vollmer et al.[25] showed a single nanoparticles would shift the resonance frequency of the WGM when in the resonator's evanescent field.

Hollow WGRs are interesting because they provide a region inside the WGR where the light can interact with the contained substance[16]. Since this region is inside of the curved surface, the fields are propagating waves with maxima located inside the WRG but not in the glass guiding structure.

Ward et al.[10, 58] showed that during carousel motion, the resonance frequency shifted when in proximity of the tapered fiber, indicating a stronger interaction between the field and the particle. A picture of trapped nanoparticles are shown in Figure 4.1a). There are three particles in the image but only the blurred out particle is trapped and being scattered around the resonator. The tapered fiber is located behind and perpendicular to the bubble. As the nanoparticle approaches the tapered fiber, the wavelength shift as shown in Figure 4.1b) with a period of roughly 8.5 second.

This chapter describes an attempt to recreate this mode shift and show in what regimes this effect can be observed. This work was carried out in the Light Matter Interaction Unit at the Okinawa Institute of Science and Technology during an internship with the Japanese Society for the Promotion of Science. The first section describes the theory of nanoparticle trapping and nanoparticle detection by resonance shifts, followed by the fabrication of micro-bubble resonators and tapered fiber. Then the experimental and imaging setup are described. The results are then given followed by a discussion of how to improvement the sensitivity of the system to observe these effects.

4.1 Theory

For a sufficiently small tapered fiber, placed far enough from the WGR's mode, will not perturb the mode enough to noticeably break the cylindrical symmetry. If the tapered fiber is large, it will break the symmetry, creating a region where the nanoparticle interacts more strongly with the light. To describe this effect, first the force driving the nanoparticle around the trap is shown, then, that the particle can be detected near the taper using perturbation theory. This section ends with a description of how the modes differ compared to those in SNAPs due to the hollow interior and mode circular geometry.

4.1.1 Force on a Neutral Polarizable Particle

This section follows the work of Zangwill[39] to derives force on a neutral, polarizable, molecule, consisting of a collection of charged particles, interacting with a slow varying electric field. The Lorentz force on such a particle is

$$\mathbf{F} = \sum_{\alpha} q_{\alpha} \left[\mathbf{E}(\mathbf{R}_{\alpha}) + \dot{\mathbf{R}}_{\alpha} \times \mathbf{B}(\mathbf{R}_{\alpha}) \right]. \tag{4.1}$$

Where q_α is the charge of an individual particle making up the molecule, $\mathbf{E}(\mathbf{R}_\alpha)$ is the electric field at $\mathbf{R}_\alpha$, $\dot{\mathbf{R}}_\alpha$ is the velocity of the particle and $\mathbf{B}(\mathbf{R}_\alpha)$ is the magnetic field at $\mathbf{R}_\alpha$. Using the slow spatially varying field approximation and that the particles never move far from the center of mass, we Taylor expand the fields about the center of mass. Setting $\mathbf{R}_\alpha = \mathbf{R} + \mathbf{r}_\alpha$ and $\dot{\mathbf{R}}_\alpha = \mathbf{v} + \dot{\mathbf{r}}_\alpha$ for center of mass position and

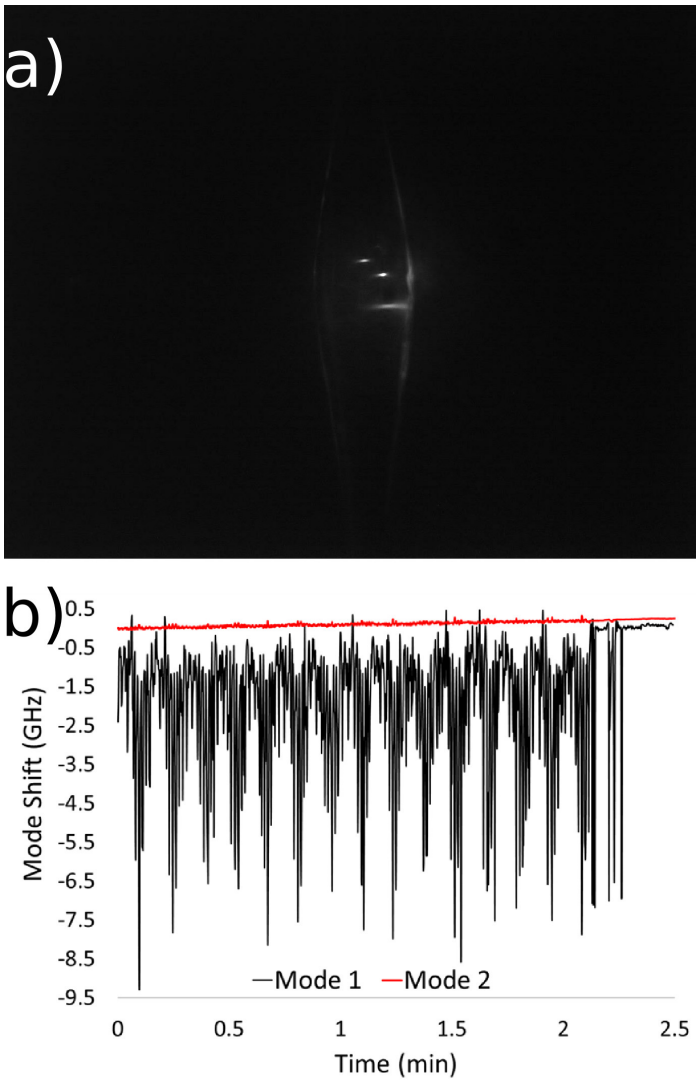

Figure 4.1: Results from a previous experiment done by Ward et al.[58] where a mode's resonance frequency shifted as a nanoparticle came in proximity of the tapered fiber. a) A few nanoparticles in a microbubble. Only one of the nanoparticles is trapped and moving around the microbubble by the scattering force. b) The resonance frequency shift during multiple periods of the particle moving around the trap. The period is roughly 8.5 seconds.

velocity $\mathbf{R}$ and $\mathbf{v}$, respectively and position and velocity relative to the center of mass $\mathbf{r}_\alpha$ and $\dot{\mathbf{r}}_\alpha$, respectively.

$$\mathbf{F} = \sum_\alpha q_\alpha(\mathbf{E} + \mathbf{v} \times \mathbf{B}) + \sum_\alpha q_\alpha(\mathbf{r}_\alpha \cdot \nabla)\mathbf{E} + \sum_\alpha q_\alpha(\mathbf{r}_\alpha \cdot \nabla)(\mathbf{v} \times \mathbf{B}) \tag{4.2}$$

$$+ \sum_\alpha q_\alpha \dot{\mathbf{r}}_\alpha \times \mathbf{B} + \sum_\alpha q_\alpha(\dot{\mathbf{r}} \cdot \nabla)(\dot{\mathbf{r}}_\alpha \times \mathbf{B}). \tag{4.3}$$

The first term is zero because the nano-particle is neutral. By the definition of a dipole moment $\mathbf{p} = \sum_\alpha q_\alpha \mathbf{r}_\alpha$ the equation can be written as

$$\mathbf{F} = (\mathbf{p} \cdot \boldsymbol{\nabla})\mathbf{E} + \dot{\mathbf{p}} \times \mathbf{B} + (\mathbf{p} \cdot \boldsymbol{\nabla})(\mathbf{v} \times \mathbf{B}) + \sum_\alpha q_\alpha(\mathbf{r} \cdot \boldsymbol{\nabla})(\dot{\mathbf{r}} \times \mathbf{B}). \tag{4.4}$$

We are only interested in the time average force on the particle. Since the optical fields are oscillating harmonically in time we only keep terms with an even number of oscillating factors of frequency ω. Since the polarizability and center of mass velocity will follow that periodicity, the two last terms will average to zero.

$$\langle \mathbf{F} \rangle = \frac{1}{2} \operatorname{Re}\{(\mathbf{p}^* \cdot \boldsymbol{\nabla})\mathbf{E} + \dot{\mathbf{p}}^* \times \mathbf{B}\}. \tag{4.5}$$

Using the definition of polarization $\mathbf{p} = \epsilon_0 \alpha \mathbf{E}$ with complex polarizability $\alpha = \alpha' + i\alpha''$. For the second term, the product rule, Ampere's Law $\boldsymbol{\nabla} \times \mathbf{E} = i\omega\mathbf{B}$ and the time independence of $\mathbf{E} \times \mathbf{B}$ gives

$$\langle \mathbf{F} \rangle = \frac{1}{2} \operatorname{Re}\{(\alpha^* \mathbf{E}^* \cdot \boldsymbol{\nabla})\mathbf{E} + \alpha^* \mathbf{E}^* \times (\boldsymbol{\nabla} \times \mathbf{E})\}. \tag{4.6}$$

We factor out the phase from the amplitude $\mathbf{E}(\mathbf{r}) = \mathcal{E}(\mathbf{r})e^{i\mathbf{k}\cdot\mathbf{r}}$ where $\mathcal{E}$ is real and, use Gauss's Law $\boldsymbol{\nabla} \cdot \mathbf{E} = \mathcal{E} \cdot \mathbf{k} = 0$ to find

$$\langle \mathbf{F} \rangle = \frac{1}{2} \operatorname{Re}\{\alpha^*(\mathcal{E} \cdot \boldsymbol{\nabla})\mathcal{E} + \alpha^*[\mathcal{E} \times (\boldsymbol{\nabla} \times \mathcal{E}) + i|\mathcal{E}|^2 \boldsymbol{\nabla}(\mathbf{k} \cdot \mathbf{r})]\}. \tag{4.7}$$

This simplifies using the vector calculus identity $\boldsymbol{\nabla}|\mathcal{E} \cdot \mathcal{E}| = 2(\mathcal{E} \cdot \boldsymbol{\nabla})\mathcal{E} + 2\mathcal{E} \times (\boldsymbol{\nabla} \times \mathcal{E})$, to

$$\langle \mathbf{F} \rangle = \frac{1}{4}\epsilon_0 \alpha' \boldsymbol{\nabla}|\mathcal{E}|^2 + \frac{1}{2}\epsilon_0 \alpha'' |\mathcal{E}|^2 \mathbf{k}. \tag{4.8}$$

These two terms are known as the gradient and scattering forces

$$\mathbf{F}_g = \frac{1}{4}\epsilon_0 \alpha' \boldsymbol{\nabla}|\mathcal{E}|^2 \qquad\qquad \mathbf{F}_s = \frac{1}{2}\epsilon_0 \alpha'' |\mathcal{E}|^2 \mathbf{k} \tag{4.9}$$

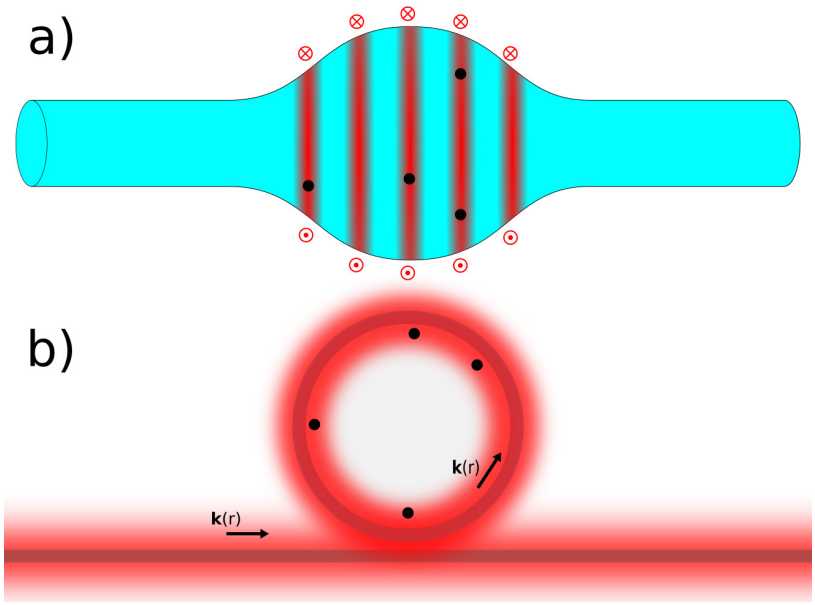

Figure 4.2: Nanoparticle trapped and scattered in bottle modes. a) Nanoparticles trapped at caustics. b) Nanoparticles trapped near the inner edge of the resonator while being accelerated in the direction of the wave vector.

The gradient force is always in the direction of the local maximum electric field which traps the particle at the field maximum. The scattering force is due to Mie scattering which transfers the optical energy and momentum to the particle. In a microbubble, the gradient force will trap the nanoparticle near the inner edge, at one of the caustics, while the scattering force will push the particles around the in carousel motion as shown in Figure 4.6.

4.1.2 Resonance Shift

The resonance shift is caused by the electric field interacting with a material of different polarizability and therefore changes the mode's optical path length. If the particle is small enough and the difference in polarizability small compared to the surrounding medium, the shift in resonance frequency can be treated as a perturbation[59]. Using a semi-classical model the perturbation is the time averaged excess energy required to polarize the particle

$$\hbar\Delta\omega = -\frac{1}{2}\langle\Delta\mathbf{p}^*\mathbf{E}\rangle_t = -\frac{1}{4}\,\mathrm{Re}\{\Delta\alpha\mathbf{E}^*\mathbf{E}\}. \tag{4.10}$$

Where $\hbar$ is Plank's constant, $\Delta\omega$ is the frequency shift, $\Delta\mathbf{p}$ and $\Delta\alpha$ are the excess dipole moment and polarizability compared to the surrounding medium. The total energy in the mode is similarly given by

$$\hbar\omega = \frac{1}{2}\int \epsilon(r)\mathbf{E}^*\mathbf{E}\mathrm{d}V. \tag{4.11}$$

Dividing these two equations gives the fractional resonance shift.

$$\frac{\Delta\omega}{\omega} = \frac{\mathrm{Re}\{\Delta\alpha\mathbf{E}^*\mathbf{E}\}}{2\int \epsilon(r)\mathbf{E}^*\mathbf{E}\mathrm{d}V} \tag{4.12}$$

In the case at hand, the shift occurs when the nanoparticle, with the slightly different polarizability $\Delta\alpha$, enters the region of larger electric field, near the tapered fiber.

4.1.3 Microbubble Resonators

The modes in a microbubble are different compared to the results from Chapter 2. The first difference arises from the microbubbles more spherical shape. For this reason, separation of variables in spherical coordinates is used [38] and the differential equation becomes

$$\frac{1}{R(r)}\frac{\partial^2 F(r)}{\partial r^2} + \frac{1}{\Phi(\phi)r^2\sin^2\theta}\frac{\partial^2\Phi(\phi)}{\partial\phi^2} + \frac{1}{\Theta(\theta)r^2\sin\theta}\frac{\partial}{\partial\theta}\left(\sin\theta\frac{\partial\Theta(\theta)}{\partial\theta}\right) = -k^2, \tag{4.13}$$

where the field is assumed to have the form

$$\mathbf{E}_r(\mathbf{r}) = R(r)\Phi(\phi)\Theta(\theta)\hat{\theta}. \tag{4.14}$$

For the angular coordinates, this leads to the well known solution of spherical harmonics

$$\Phi(\phi)\Theta(\theta) = \left[P_n^m(\cos\theta)\right]\left[\cos\theta\right]. \tag{4.15}$$

Where $P_n^m(x)$ are the Legendre polynomials. For the radial function, the different refractive index at the center region of the microbubble means there will be a second matching condition which is treated in the same way as the other. The piecewise solution is [37]

$$R(r) = \begin{cases} AJ_{m+1/2}(k_0 n_{water} r) & , r \le R_1(z) \\ BJ_{m+1/2}(k_0 n_{glass} r) + CH^{(2)}_{m+1/2}(k_0 n_{glass} r) & , R_1(z) < r \le R_2(z) \\ DH^{(2)}_{m+1/2}(k_0 n_{air} r) & , r > R_2(z) \end{cases}. \tag{4.16}$$

Where the Bessel and Hankel function are of half integer order. The coefficients A,B,C,D are determined by the boundary conditions,

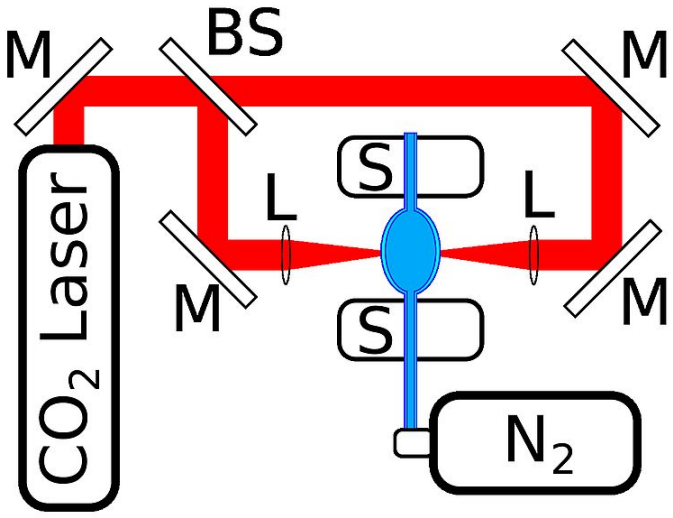

Figure 4.3: Microbubble fabrication setup. M: mirror, BS: beam splitter, S: stage, L: lens, N_2: high pressured nitrogen. First the laser heats a capillary fiber while stages pull, elongating the capillary. Second, the laser heats the capillary while high pressure nitrogen gas is pumped in, inflating the microbubble.

4.2 Fabrication

The method used to fabricate the microbubble was developed by Yang et al.[20] and consisted of pumping high pressure gas in a capillary fiber while heating with a CO_2 laser. Fabrication of tapered fiber was the same described in Section 3.1.1

4.2.1 Microbubbles

A schematic of the microbubble fabrication setup can be seen in Figure 4.3. A CO_2 laser was used to heat the capillary above the glass transition temperature, making it malleable. The beam is split into two, and guided to heat the capillary from either side, providing uniform heat and canceling radiation pressure effects. There are two stages holding the capillary in place. One of which is fixed and the other can moves linearly, pulling the capillary.

Starting with a capillary of 250 μm inner diameter and 350 μm outer diameter. The first step consists of heating the capillary with the laser while the movable stage pulls, reducing the diameter to approximately 18 μm. The second step consists of pumping compressed nitrogen gas into the capillary while heating the previously thinned out region. The softened glass and pressure difference causes the bubble to

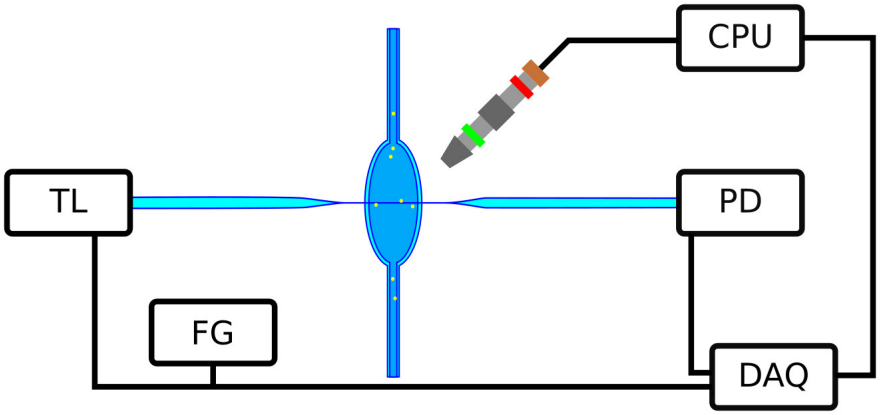

Figure 4.4: Nanoparticle trapping and sensing setup. TL: Tunable laser, FG: Function generator CPU: computer, PD: photodiode, DAQ: data acquisition card. The computer is connected to a camera.

inflate at a rate controllable by the laser power. Once the desired size is reached, the bubble is mounted in the same manner as the taper.

4.3 Experimental Setup

A schematic of the experimental setup can be viewed in Figure 4.4. A laser with center wavelength at 780nm scans over over a wavelength range, sending the light down the tapered fiber to couple light in and out of the microbubble modes. The transmitted light reaches the photodiode and an electrical signal is sent to a National Instrument data acquisition card (DAQ). To scan the laser frequency, a function generator was split, sending part of a ramp signal to a modulation input of the laser and the other part to the DAQ for triggering and wavelength calibration.

A solution of distilled water with a low concentration of 500 nm polystyrene nanoparticles was pumped into the microbubble using a syringe. A very small pressure difference will produce a small flow through the microbubble. With the laser is on, the a nanoparticle would enter the microbubble and become trapped in the mode.

For imaging, the nanoparticles were doped, by the manufacturer, to fluoresce. As shown in Figure 4.5, 532nm laser light is reflected off a dichroic mirror before exciting the fluorescent nanoparticles. The nanoparticles emit 570nm light back towards the dichroic mirror, which will pass though to reach the CCD camera. Two filters were

used to block any unwanted scattered light. A band-pass filter was placed between the mirror and the microbubble to block everything but the 532nm and 570nm, and a low-pass filter was placed just before the camera to block out any scattered 532nm light.

4.4 Results and Outlook

The nanoparticles were trapped, and propelled around the microbubble but no mode shift or acceleration of the particle was observed when passing near the tapered fiber. One reason this experiment may have failed is due to the small regime of optical power. At low power, the light may not trap the nanoparticle strongly enough to keep it near the electric field maximum, allowing the mode to shift due to Brownian motion[60]. At too large power, turbulence will prevent any steady modes from forming on the timescale required.

A possible way to circumvent this problem would be to make a larger tapered fiber to create a larger localization in that region. Conversely, instead of increasing the fields, the sensitivity could be increased by using a mode locking technique that would allow much smaller resonance shifts to be measured.

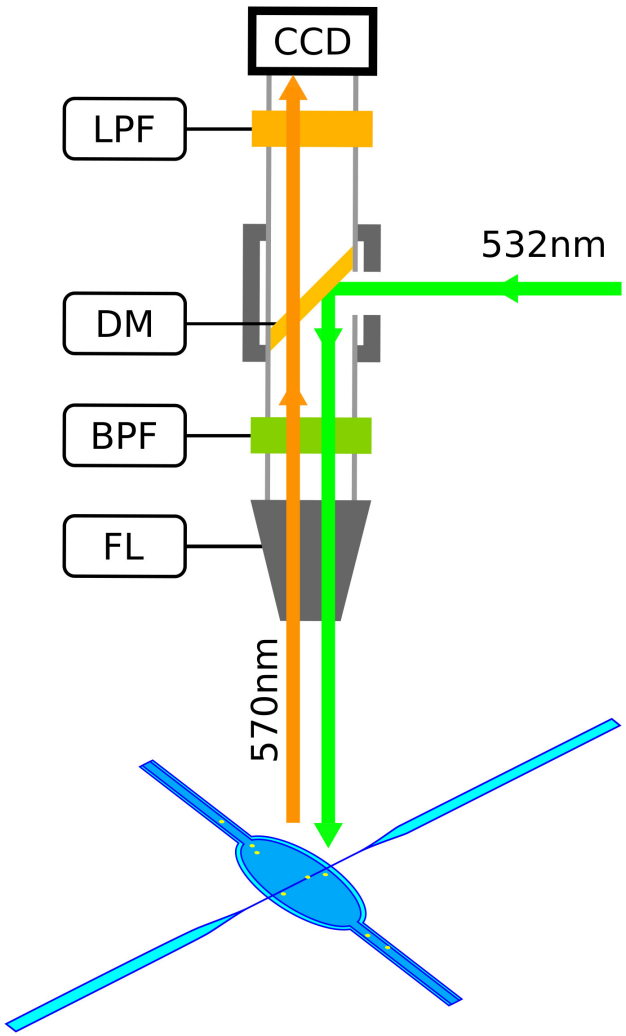

Figure 4.5: Camera used for imaging the trapped nanoparticles. 532nm light is reflected off a dichroic mirror to excite the fluorescent nanoparticles. The lower frequency light passes the mirror and landing on the CCD camera. A filters was used between the mirror and nanoparticles, and another between the mirror and CCD sensor to block out any unwanted light.

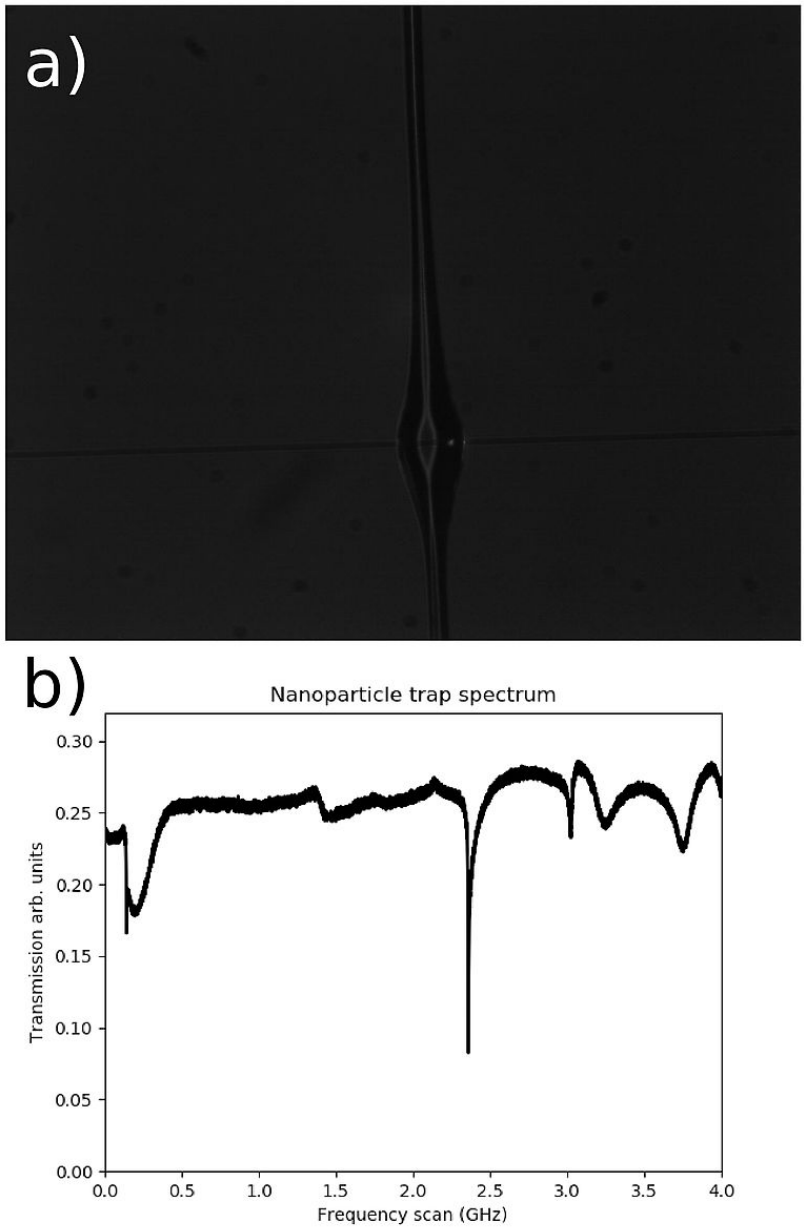

Figure 4.6: Data from a nanoparticle trapped near the inner edge of a microbubble. a) Image of the fluorescent nanoparticle, propelled by the scattering force. b) Spectrum showing the mode trapping the nanoparticle.

Chapter 5

Locking to a Mode

5.1 Introduction

Locking a laser to a cavity mode is a useful technique, both for stabilizing a laser and for tracking changes in resonance frequency. The best method known today is the Pound-Drever-Hall technique[61], which uses frequency modulation to measure how far off the laser is from resonance, and feeds that signal back to laser for correction.

In order to lock a laser to a mode, we need a error signal, a linear function of frequency with a non-zero slope to indicate which side of resonance the laser is on. Older techniques would lock the transmitted or reflected light to the a value near the midpoint of the intensity, where the slope is large. The problem with this method is that on cannot differentiate between changed in frequency and changes in power. The advantages of the Pound-Drever-Hall technique is that the corrections always brings the error signal to zero, decoupling the signal from the power fluctuations[62]. Secondly, because this technique is based on lock-in detection, the frequency modulation can be chosen at a frequency such that the noise spectral density is low, avoiding many sources of noise completely.

When used to track a resonance, the lock is particularly useful for resolving the resonance much more accurately and at much higher sampling rate than by measuring the transmission during sequential scans[61].

Applying this technique to chapter 3, given an adequate theoretical model, would allow more precise measurements of the mode's refractive index and measurements of the radius. Since these two parameters are measured in sensing applications, as in

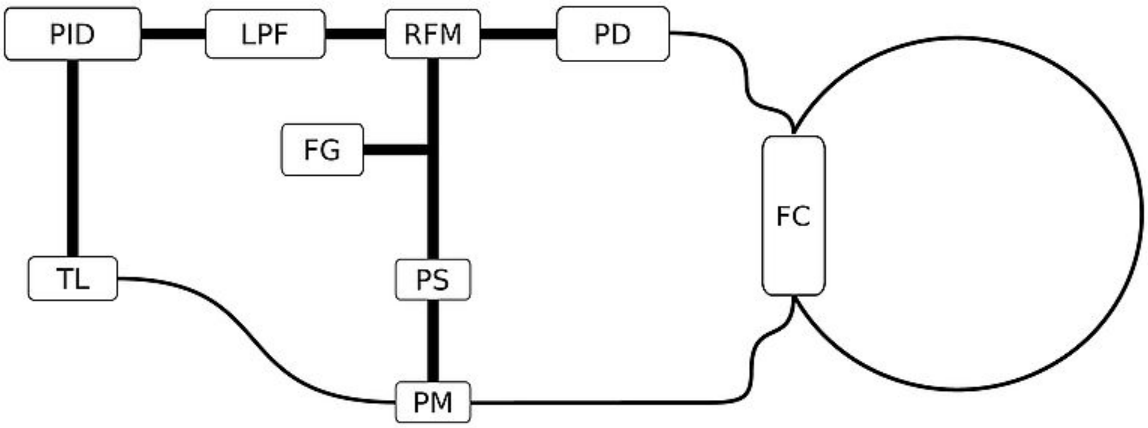

Figure 5.1: Pound-Drever-Hall feedback loop for locking a laser to a cavity. Thick lines represent electrical connection while thin lines represent optical fiber.PID: proportional integral differential, LPF: low pass filter, RFM: radio frequency mixer, PD: Photo-diode, FG: function generator, PS: phase shifter, PM: phase modulator, TL: tunable laser, FC fiber coupler.

chapter 4, it improves the resolution of sensors.

In this chapter, the Pound-Drever-Hall technique is theoretically explained and the results of a laser locking to a fiber ring resonator are shown. Locking to a fiber ring resonator was advantageous because it is a more robust platform than ones involving a tapered fiber. This technique can easily be applied to SNAPs or microbubbles by replacing the fiber ring with a tapered fiber and a SNAP or microbubble.

5.2 Theory

This section theoretically describes the Pound-Drever-Hall technique. Closely following the original paper by Drever et al.[61] and the work of Black[62] starting with frequency modulation, lock-in detection(mixing and low pass filter), feedback amplification and noise analysis.

5.2.1 Error Signal

The basic setup for a Pound-Drever-Hall lock is shown in Figure 5.1. Starting at the laser, light is sent towards the phase modulator with an electric field

$$E = E(x)e^{i\omega t}. \tag{5.1}$$

The light passes through the phase modulator and emerges with an electric field[62]

$$E = E(x)e^{i(\omega t+\beta\sin(\Omega t))}. \tag{5.2}$$

Where β is the modulation depth and Ω is the modulation frequency. Using the Fourier-Bessel expansion, this can be expressed as

$$E \approx E(x)[J_0(\beta) + J_1(\beta)2i\sin(\Omega t)]e^{i\omega t} \tag{5.3}$$

$$E \approx E(x)[J_0(\beta)e^{i\omega t} + J_1(\beta)e^{i(\omega+\Omega)t} - J_1(\beta)e^{i(\omega-\Omega)t}] \tag{5.4}$$

using Euler's identity in the last step. This approximation is valid if the modulation depth is near 1. This value is chosen such that only the zeroth and first order Bessel functions have significant contributions and higher order sidebands can be neglected. Expressed this way, it appears as three beams of light are incident on the cavity, a carrier at frequency ω and two sidebands at frequencies $\omega\pm\Omega$. The time and frequency domain plots of this can be seen in Figure 5.2. Note that despite the multiple beams of light, there is no beating of the whole signal.

The carrier and sidebands couple in and out of the cavity, interacting with the cavity independently. The emerging field is given by the sum of each frequency, carrier and sidebands, multiplied by the transfer function, Equation (2.45), at the respective frequencies. The emerging field is

$$E \approx E(x)[F(\omega)J_0(\beta)e^{i\omega t} + F(\omega+\Omega)J_1(\beta)e^{i(\omega+\Omega)t} - F(\omega-\Omega)J_1(\beta)e^{i(\omega-\Omega)t}] \tag{5.5}$$

Where $F(\omega) = E_3/E_1$ is the transfer function at frequency ω. The Power is proportional to the square of the electric field[62].

$$\begin{aligned} P =& P_c|F(\omega)|^2 + P_s\left[|F(\omega+\Omega)|^2 + |F(\omega-\Omega)|^2\right] && (5.6)\\ &+2\sqrt{P_cP_s}\,\mathrm{Re}\left[F(\omega)F^*(\omega+\Omega) - F^*(\omega)F(\omega-\Omega)\right]\cos(\Omega t) && (5.7)\\ &+2\sqrt{P_cP_s}\,\mathrm{Im}\left[F(\omega)F^*(\omega+\Omega) - F^*(\omega)F(\omega-\Omega)\right]\sin(\Omega t) && (5.8)\\ &+(2\Omega \text{ terms}) && (5.9) \end{aligned}$$

Where P_c and P_s is the power in the carrier and each sideband, respectively. The important terms are those proportional to $\sin(\omega t)$ and $\cos(\omega t)$. These terms can be interpreted as the carrier beating with one of the side-bands while the ignored terms,

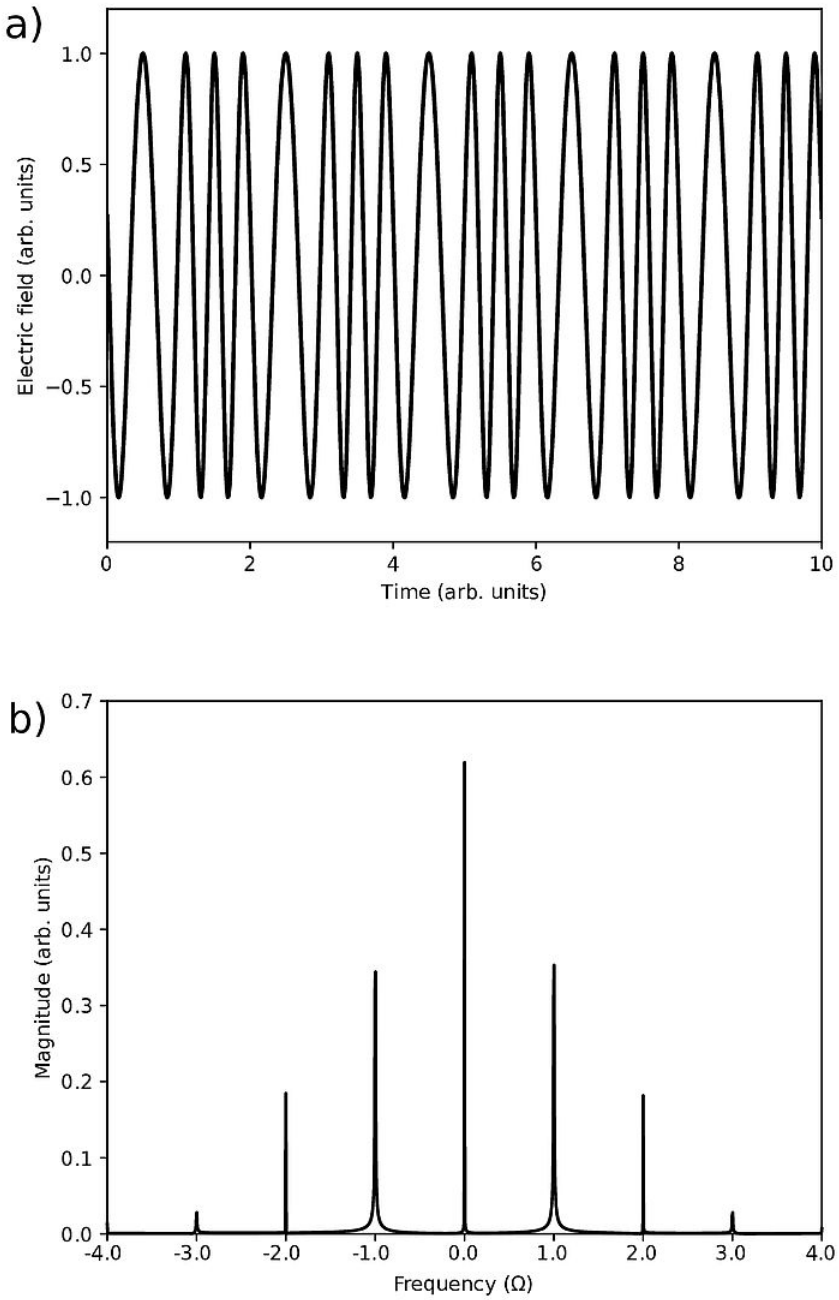

Figure 5.2: Electric field of a phase modulated light in: a) the time domain and b) the frequency domain. When there is only phase modulation, no amplitude modulation is observed.

proportional to $\sin(2\omega t)$ and $\cos(2\omega t)$ are due to the two side-bands beating together. While on resonance, the beating of both sidebands with the carrier cancel out, but as the carrier moves away from resonance, some amplitude modulation will occur. As the carrier's frequency is shifted to the opposite side of resonance, the modulation is be 180° radians out of phase. This beating is slow enough that the photodiode can follow, and send the signal to the mixer. The mixer multiples this signal with the reference signals from the function generator. If the reference signal is in phase with the $\cos(\Omega t)$ term, the output will be

$$\begin{aligned} V_m =& V_r \left(V_c|F(\omega)|^2 + V_s\left[|F(\omega+\Omega)|^2 + |F(\omega-\Omega)|^2\right]\right)\cos(\Omega t) && (5.10)\\ &+2V_r\sqrt{V_cV_s}\,\mathrm{Re}\left[F(\omega)F^*(\omega+\Omega) - F^*(\omega)F(\omega-\Omega)\right]\cos^2(\Omega t) && (5.11)\\ &+2V_r\sqrt{V_cV_s}\,\mathrm{Im}\left[F(\omega)F^*(\omega+\Omega) - F^*(\omega)F(\omega-\Omega)\right]\sin(\Omega t)\cos(\Omega t) && (5.12)\\ &+(\Omega \text{ and } 3\Omega \text{ terms}) && (5.13) \end{aligned}$$

Where V_m is the mixer output voltage, V_r is the voltage of the reference signal, V_c and V_s are the voltages from the photodiode associated with the carrier and sideband power. Using trigonometric identities this becomes

$$\begin{aligned} V_m =& V_r \left(V_c|F(\omega)|^2 + V_s\left[|F(\omega+\Omega)|^2 + |F(\omega-\Omega)|^2\right]\right)\cos(\Omega t) && (5.14)\\ &+V_r\sqrt{V_cV_s}\,\mathrm{Re}\left[F(\omega)F^*(\omega+\Omega) - F^*(\omega)F(\omega-\Omega)\right](1+\cos(2\Omega t)) && (5.15)\\ &+V_r\sqrt{V_cV_s}\,\mathrm{Im}\left[F(\omega)F^*(\omega+\Omega) - F^*(\omega)F(\omega-\Omega)\right]\sin(2\Omega t) && (5.16)\\ &+(\Omega \text{ and } 3\Omega \text{ terms}) && (5.17) \end{aligned}$$

The low pass filter is set with a cutoff frequency to remove all but the DC component, leaving

$$V_{er} = V_r\sqrt{V_cV_s}\,\mathrm{Re}\left[F(\omega)F^*(\omega+\Omega) - F^*(\omega)F(\omega-\Omega)\right]. \tag{5.18}$$

Where V_e is the error signal. If the reference signal was shifted by a 90° to be in phase with the imaginary term, a similar calculation would give

$$V_{ei} = V_r\sqrt{V_cV_s}\,\mathrm{Im}\left[F(\omega)F^*(\omega+\Omega) - F^*(\omega)F(\omega-\Omega)\right]. \tag{5.19}$$

When the modulation frequency is less than the cavity linewidth, V_{er} gives a more desirable error signal and when the modulation frequency is larger than the linewidth, V_{ei} is more desirable[62]. For the interested reader, a thorough study of the error

signal for the two phase relations, at different modulation frequencies can be seen in Bjorklund et al. work[63]. Both cases are plotted as a function of the relative carrier frequency from resonance in Figure 5.3.

Up to this point, we've described frequency modulation spectroscopy, using the error signal given in Figure 5.3 we can determine resonances with much more precision than from a Lorantzian peak. For the Pound-Drever-Hall technique, we are interested in working near resonance, where the signal is approximately linear and the slope is large. Around that point, small mismatches in resonance will produce a large voltage at the low pass filter output. This voltage is then amplified by the PID controller and fed into one of the laser's modulation input, correcting the laser's wavelength to match the cavity's resonance. The voltage output of the PID can also be used as a readout of the laser's wavelength since there is a linear relation between the applied voltage and the laser's wavelength.

The PID controller takes the error signal from as an input and outputs the voltage given by

$$V_{out} = k_p V_{in}(t) + k_i \int_0^t V_{in}(t')\mathrm{d}t' + k_d \frac{\mathrm{d}V_{in}(t)}{\mathrm{d}t} \tag{5.20}$$

The k_p, k_i and k_d are the proportional, integral and differential constant coefficients. k_p makes high frequency correction, k_i tracks the mode when the frequency changes, as it would typically do in sensing applications and k_d prevents overshooting the zero point error. When the frequency corrections are always small, k_d can be set to zero.

5.2.2 Noise

The closed loop noise spectral density dictates how closely the laser can match the resonance and is given by[64]

$$S_{f,cl} = \frac{\sqrt{s_{f,laser}^2 + |KS_{v,PID}|^2 + |Kk_pS_{v,error}|^2}}{|1 + Kk_pD_v|} \tag{5.21}$$

Where $S_{f,cl}$ and $S_{f,laser}$ are the closed loop and laser's, noise spectral density noise, respectively, in dimensions of frequency. $S_{V,PID}$ and $s_{V,error}$ are the PID and error signal's, noise spectral density noise, respectively, with dimensions of voltage. K is the laser input's modulation frequency coefficient, and D_v is the slope of the error signal at resonance.

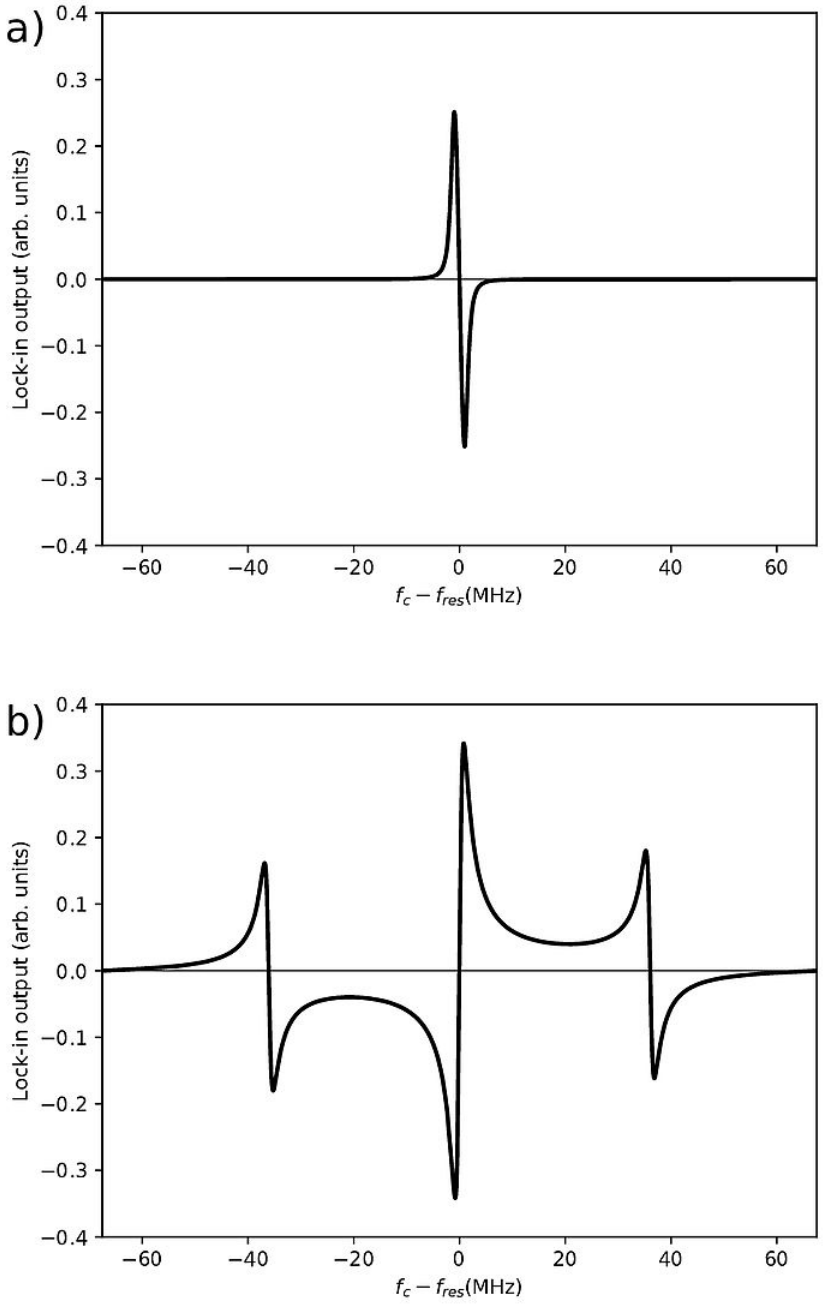

Figure 5.3: Error signals for different modulation frequencies. a) The modulation frequency is less than the mode's linewidth and the reference is in phase with the $\cos(\Omega t)$ term. b) The modulation frequency is larger than the resonance and the reference signal is in phase with the $\sin(\Omega t)$ term.

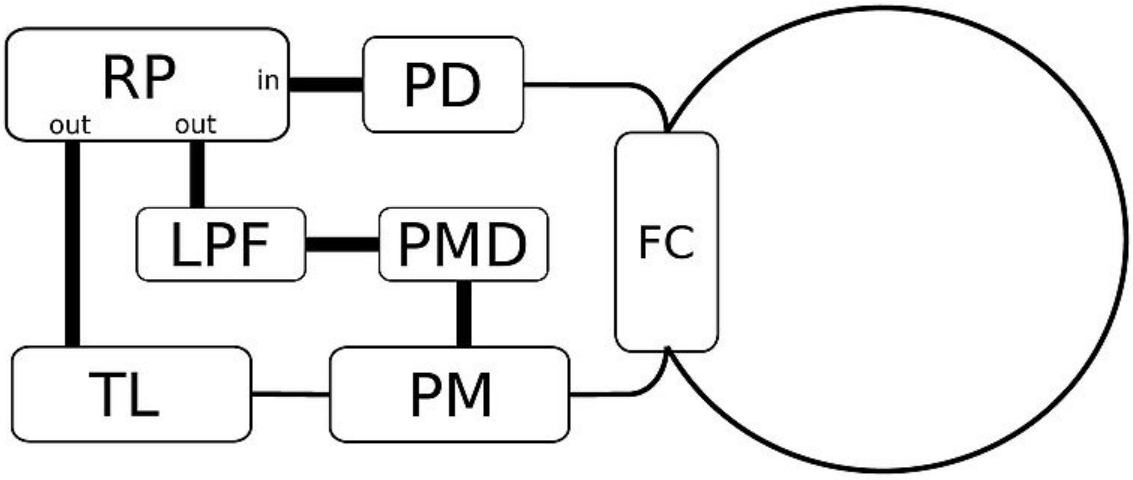

Figure 5.4: Experimental setup, RP: Red Pitaya^{TM}, PD: photo-diode, LPF: low pass filter, TL: tunable laser, PM: phase modulator, PMD: phase modulator driver, FC: fiber coupler

We can see that if the gain of the PID, K_p, is very large, this equation is approximately

$$S_{f,cl} = \frac{S_{v,error}}{D_v} \tag{5.22}$$

In this regime, the only source of error is from the error signal output. In the best case, this will be dominated by the shot noise of the photons on the photodiode[62] but can also be dominated by the electronic noise in the photodiode, lock-in amplifier or from poorly chosen modulation and cut-off frequency.

5.3 Experimental set-up

Figure 5.4 shows a schematic of the setup and table 5.1 shows the list of equipment. The ring resonator was fabricated by splicing two ends of the 99/1 fiber coupler such that the ends coupling 99% are fused together. The resonance peaks have a FWHM of 3.2 MHz as shown in Figure 5.5. For this linewidth, the slow and fast modulation frequencies were chosen to be 2MHz and 31MHz, respectively.

Many of the components were digitally embedded in the Red Pitaya^{TM} (RP), a single board computer with two input and two output field programmable gate arrays (FPGA). The program used was the open source Lock-in+PID program, which can be installed through the RP Marketplace. This program, written by Luda et

Component	Manufacturer	Model
Tunable laser	GN-Nettest	TUNICS-plus 3644HE-15
Polarization controller	OZ Optics	FPC-100
Photo detector	Thorlabs	PDA 10CF
FPGA signle board compter	Red Pitaya^{TM}	Stemlab125-14
Low pass filter	Minicircuits	BLP-1.9+ (slow modulation) BLP-27+ (fast modulation)
Fiber coupler	Thorlabs	PNH1550R1A2
Phase modulator	iXBlue	MPX-LN-0.1
Phase modulator driver	iXBlue	DR-VE-0.1-MO

Table 5.1: List of components used in experimental setup (Figure 3.4).

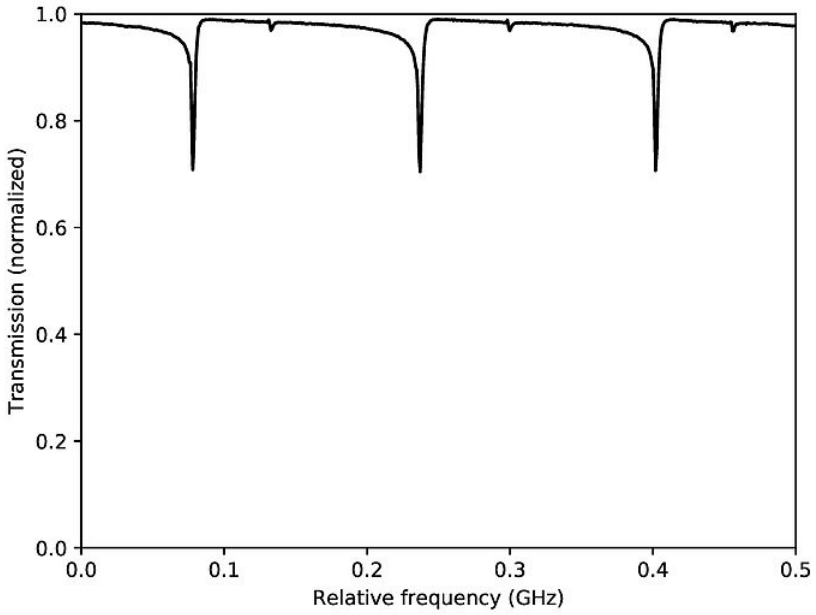

Figure 5.5: Fiber ring spectrum. Modes have a full width half maximum of 3.2MHz corresponding to a Q-factor of 60 million.

la. [65], includes a lock-in amplifier(function generator, mixer, low pass filter) and proportional-integral-derivative(PID controller). It also includes tools to help set up the lock including a ramp scan generator, oscilloscope and Lock Controller. These components are controlled over the network through an internet browser. Screenshots of the graphical user interface(GUI) can be seen in Figure 5.6 and Figure 5.7 .

Input 1 was connected to the photodiode signal, output 1 was the sending the lock-in's modulation signal to the phase modulator and output 2 was sending the Lock Controller signal to the laser. For the modulation frequencies we were working with, we used the fast, square wave, modulation. This was needed because a sinusoidal function is more difficult to implement electronically at high frequencies[66]. However, thought of as a Fourier series, a square wave is a sum of sinusoidal waves. The higher harmonics, if not removed, will produce extra sidebands that interfere with the desired signal. These frequencies were therefore removed with the low pass filter which was connected between output 1 of the RP and the phase modulator driver. The modulation signal was then amplified to produce a modulation depth near 1.

To set up the lock, the RP oscilloscope displayed the error signal and the ramp scan for triggering. The lock-in amplifier's modulation frequency was set to the desired frequency, either 2MHz or 31MHz. The ramp scan was then set to a frequency of 50Hz with maximum amplitude. The Lock Controller was set to output the ramp signal to the laser,displaying the error signal on the oscilloscope. The lock-in amplifier's low pass filter's cutoff frequency was set just low enough to be remove any noticeable modulation in the error signal, 100kHz. Lastly, the phase was adjusted to achieve the desired error signal as in 5.3.

In the PID module, the error offset set to make the average error zero, as indicated on the right side of the Figure 5.6 . In our case, the slope of the error signal was positive during the upwards scan meaning the PID coefficients should be positive [1]. The proportional coefficient (k_p) was set to have a maximum value which didn't clip the error signal at the RP output (1V). The integral coefficient (k_i) was set to its minimum non-zero value and increased after locking just below the value when it became unstable. The derivative coefficient was set to zero.

The Lock Controller initially sent the ramp signal to the laser, scanning over a wavelength range. The module was set to monitor the error signal and was triggered

[1]The program includes an overall negative sign in the PID

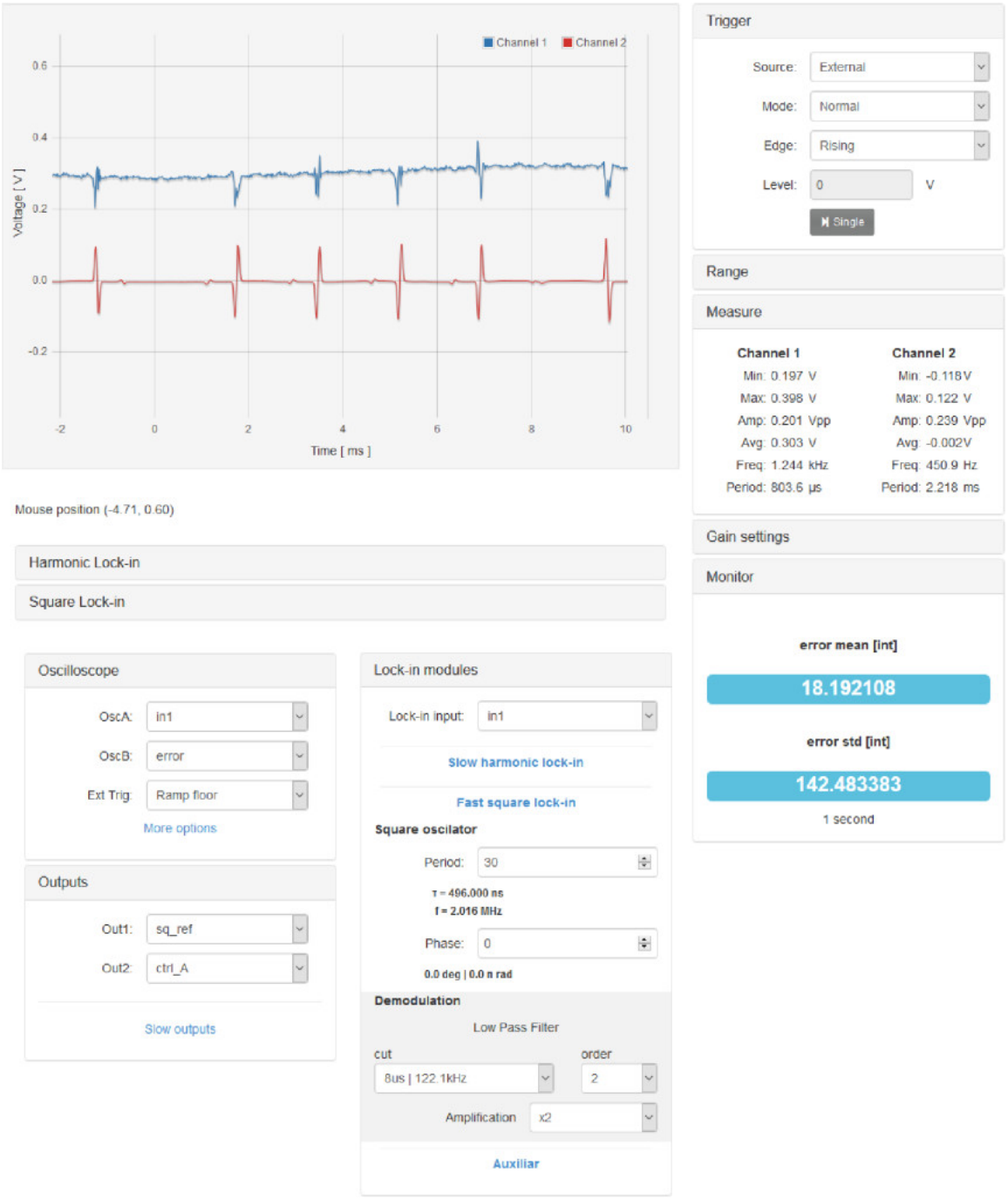

Figure 5.6: Part of the graphical user interface for Lock-in+PID program. The electrical signal from the photodiode is sent to the lock-in amplifier which outputs the error signal to the PID controller (next figure). The oscilloscope is used to set all the parameters. The oscilloscope shows the photodiode input and error signal during a ramp scan. The 4 modes in the center are during the upwards scan while the two on the side are during downwards scans as seen by the slope direction change.

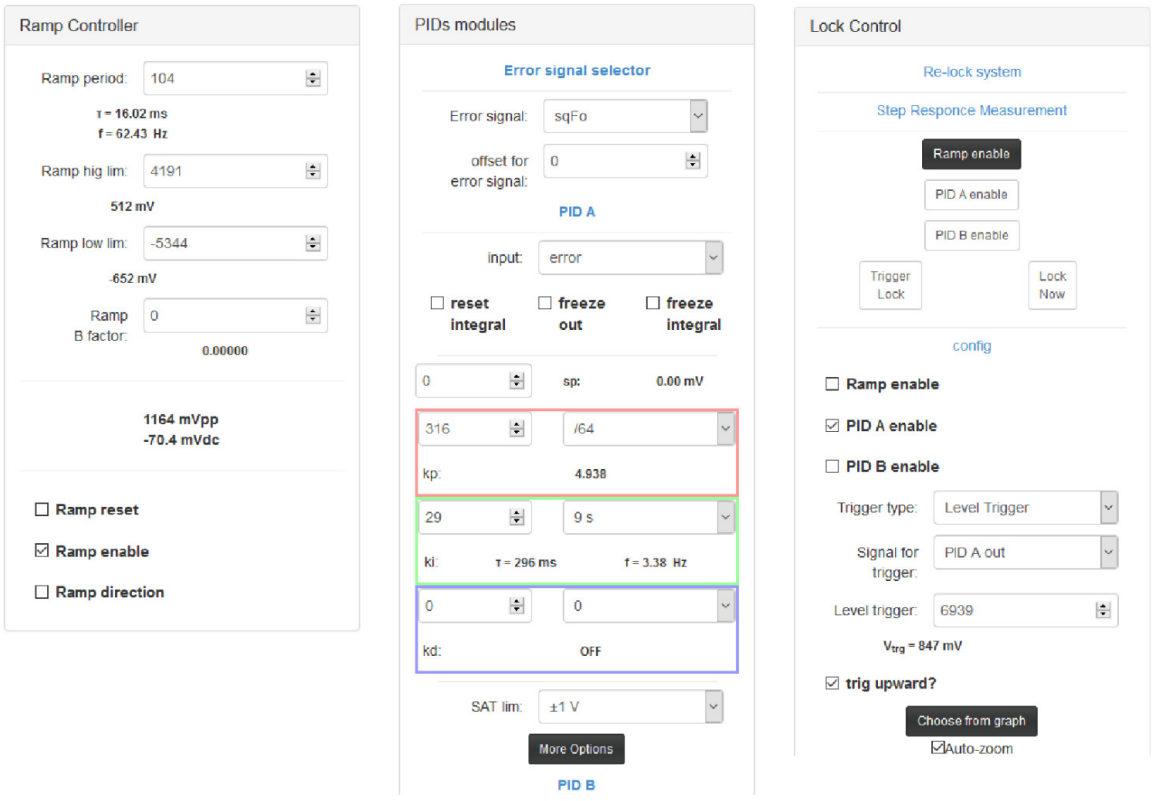

Figure 5.7: Part of the graphical user interface for Lock-in+PID program. The Ramp Controller is used to scan the laser's wavelength while tuning the lock-in amplifier parameters until the error signal looks like Figure 5.3 on the internal oscilloscope. The PID module receive the error signal from the lock-in amplifier and is fed back to the laser. The Lock Controller switches the output going to the laser's modulation input, from the Ramp Controller to the PID module when the carrier is close to resonance enough to lock.

when error signal was near a maxima. At that point the Lock Controller switches the output from the ramp to the PID controller.

It's worth pointing out that in the slow modulation case, the laser will automatically lock to a mode without the lock control and that even if it unlocks, it will automatically re-rock to that, or another mode. When the modulation is fast, the laser will re-lock to resonance as long as the cavity frequency remains within the two sidebands. This can be seen by the fact that the error signal always has the correct sign to push it in the right direction.

5.4 Results

The error signal for both slow and fast modulations are shown in Figure 5.8. When the PIDs were activated, the lock is working when the error signal mean and standard deviation are reduced to zero. The values can be read off the GUI as seen on the right side of Figure 5.7

5.5 Outlook

Locking was achieved but certain modifications can be made to improve the lock. First, the PID output signal would need to be amplified. Since the RP can only output $\pm 1V$, amplification would ensure that most of the noise is suppressed and the spectral density is accurately described by Equation (5.22).

A second improvement would be to condition the signal between the photodiode and the RP input. Since the only part of the signal that matters are the terms oscillating at the modulation frequency, a bandpass filter would remove any unnecessary parts of the signal. Removing these unnecessary terms would allow the range of the RP 14 bit ADC to be detracted to the relevant modulation terms.

This mode locking technique could detect much smaller wavelength shifts in the nanoparticle trapping experiment. Applying this lock to Chapter 3 would give a more accurate value for wavelength shifts in real time. The spectrogram gives a nice visual to identify the mode numbers and polarization but once that has been determined, only two modes of orthogonal polarization are needed. This could be used to improve sensing and differentiate between temporal changes in the refractive index and the

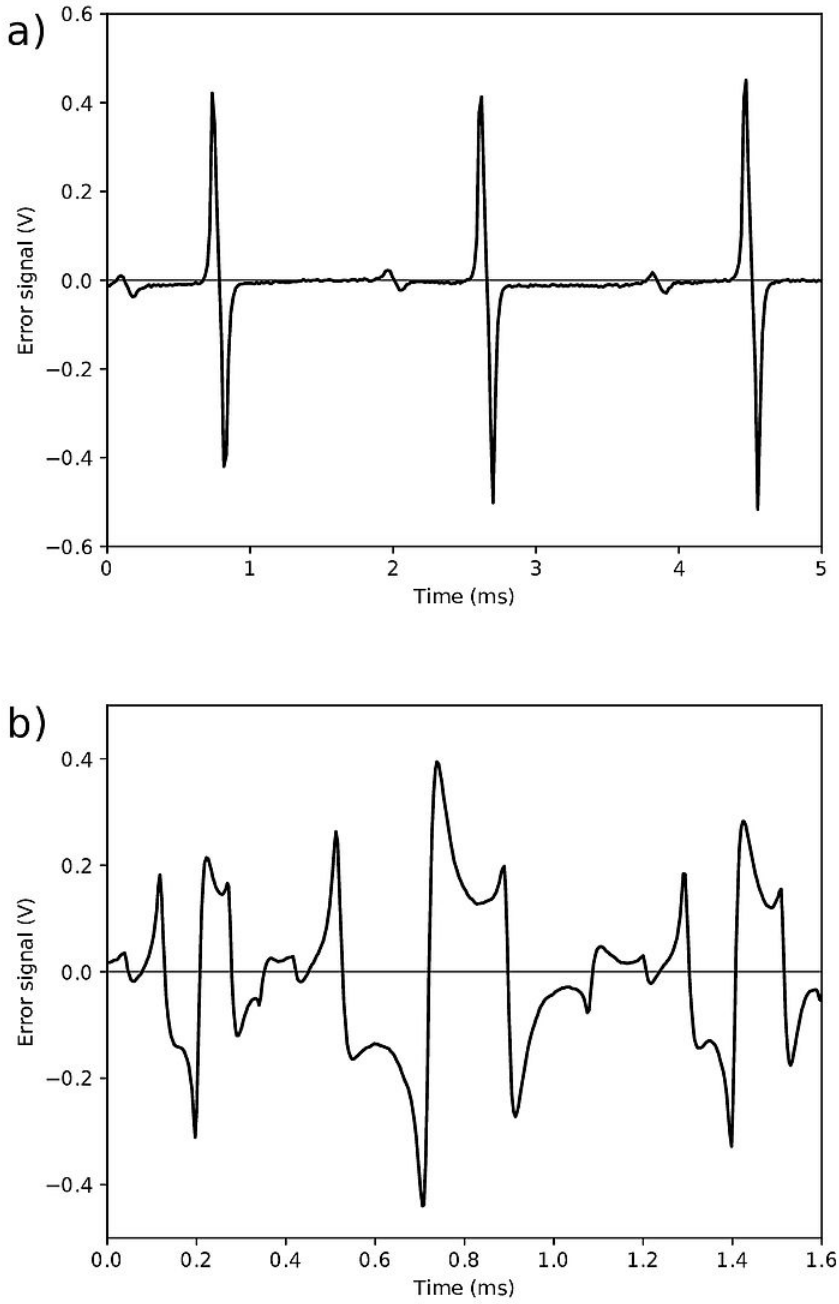

Figure 5.8: The error signal during a ramp scan for a) 2MHz modulation and b) 32MHz modulation. a) the small error signals that appear between the large signals are mode of orthogonal polarization. b) For each mode, the expected Pound-Drever-Hall signal can be seen with the addition of the second order sideband crossing the axis on the outside of the Pound-Drever-Hall signal. The signal in a) use a more stable laser (Rio Orion 1550 nm Laser Module) The signal in b) is quite unstable and would stabilize once locked.

radius.

Chapter 6

Packaging of Surface Nanoscale Axial Photonic Resonators

Throughout this thesis, light was coupled into the resonator through a tapered fiber. This method is preferred due to the tapered fiber's strong evanescent field and easy of alignment but, suffers from the fragility of the fiber, which breaks easily.

Another issue, related to the SNAP itself, is scattering due to a monolayer of silanols that bind to the surface. Shortly after fabrication atmospheric water in the proximity of the surface will chemisorb to the surface as shown in Figure 6.1a). Two hydroxide groups will be left bonded to the surface, creating a dipole. This dipole will then adsorb to more atmospheric water[67] as shown in Figure 6.1b).

These layers scatter light, therefore reducing the Q. It was also shown that the Q factor could be partially restored by heating the resonator[40].

This chapter describes an attempt to address both these issues. Packaging was designed, fabricated and tested to hold a coupled SNAP and tapered fiber as a two port device. The packaged device was first tested against impact for its durability. Then subjected to heat and vacuum to remove the layer of water in an attempt to partially restore the Q factor.

6.1 Fabrication

The packaging was designed with a computer aided design software and printed with a 3D printer. It consists of 2 parts: a base to which the SNAP and taper are epoxied

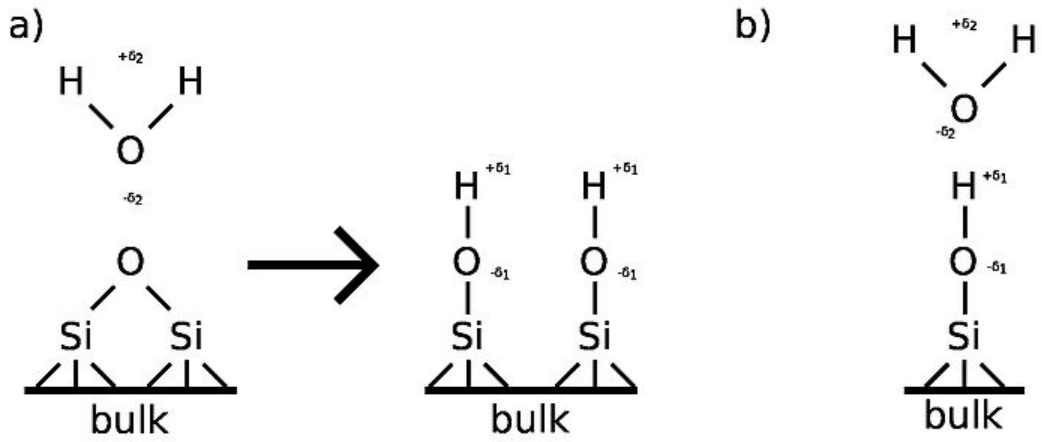

Figure 6.1: a) Atmospheric water will chemosorb to the surface, producing to produce silanols. b) The dipole in due to a silanol will adsorb atmospheric water[67].

to, and a lid, glued on top, to protect the components as shown in Figure 6.2a).

There are 4 steps in the fabrication. First, the tapered fiber is fabricated is described in Chapter 3 but with the mount replaced by the new base as seen in Figure 6.2b). For the vacuum experiment, the epoxy was degassed before curing. The second step is to fabricate a SNAP using the same method as in Chapter 3. The SNAP is then taped to a temporary mount as can be seen in Figure 6.2c). The SNAP is then positioned to couple into the desired mode with the desired coupling strength. This was done using the same experimental setup as in Figure 3.4. Once the desired parameters are obtained, the SNAP is epoxied to either edge of the base as shown in Figure 6.2c). Lastly the lip is glued to the device, shutting it as seen in Figure 6.2d).

6.2 Drop Test

The experimental setup consisted of a packaged SNAP attached to a linear rail with an accelerometer and an iron plate at one end of the rail as shown in Figure 6.3. During the duration of the test, the transmission spectrum was monitored using a tunable laser, photodiode and oscilloscope. The SNAP was drop repeatedly with increasing heights until the taper broke. Changes to the transmission were noted and the results are tabulated in Table 6.1

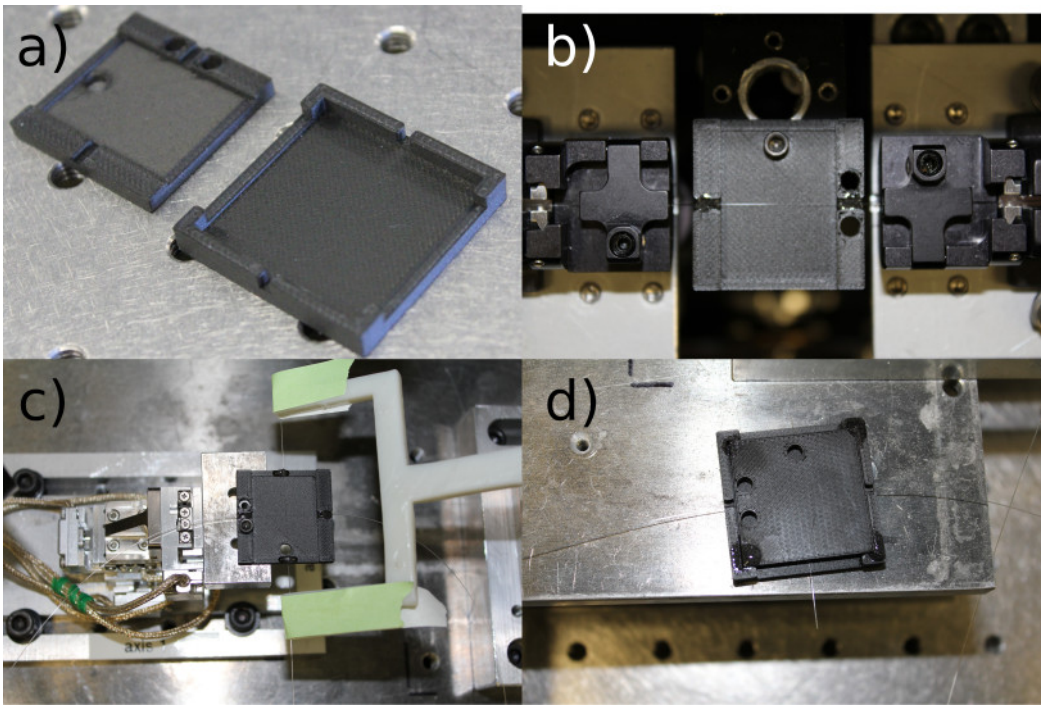

Figure 6.2: Packaging of a SNAP. a) The 3D printed mount. The base is on the left and the lid is on the right. b) Tapered fiber, epoxied to a mount while still clamped in the fiber puller's stages. c) SNAP after being positioned and epoxied to couple with the taper. The SNAP is still taped to the temporary mount. d) Final device sealed with the lid.

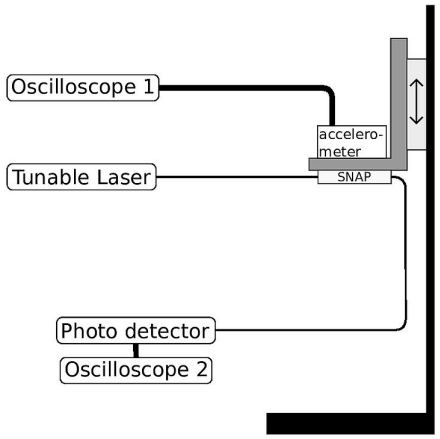

Figure 6.3: Drop test experimental setup. a) Osc: oscilloscope, acc: accelerometer, TL: tunable taser, PD: photodiode. The arrows show the directions the linear rail moves

Acceleration (height)	Result
0-140g (0-5cm)	no effect
140-280g (5-10 cm)	changed coupling
>280g (10cm)	no transmission

Table 6.1: Results from the drop test. The device was dropped from increasing heights one centimeter increments until breaking.

Temperature($^{\circ}C$)	Result
<70	no change
70-110	changed coupling
>110	broke

Table 6.2: Results from heating the fiber to remove adsorbed water vapors. The temperature was adiabatically increased while the transmission was monitored.

6.3 Dehydration

After atmospheric water was allowed to adsorb on the surface of the SNAP overnight, two methods were used to attempt to boil off the adsorbed water. First by heating and then by vacuum.

During the heating experiment, the packaged SNAP was place in a furnace while the transmission was monitored with a tunable laser, photodiode and oscilloscope. The Q factor was not noticeably improved. The coupling started to change above 70°C and broke over 110°C. The results are tabulated in Table 6.2

In the vacuum experiment, the packaged SNAP was placed in a 10 μbar vacuum, well below water's room temperature boiling point pressure of 21 $mbar$. The lack of optical fiber ports connecting to the vacuum chamber meant the spectrum could not be monitored while in the vacuum but needed to be reconnected at the laboratory pressure and humidity. Reconnecting the SNAP to the laser and oscilloscope took less than 2 minutes. The Q factors were not improved and different resonance frequencies were observed before and after, indicating that the tapered moved related to the SNAP.

6.4 Discussion and Outlook

The packaging is durable for research purposes but any impact on a hard surface, even from low height will break the tapered fiber. With some engineering and proper

choice of material, the mount could be made to dampen accelerations. For our current use, this device is robust enough for our use of transporting to different facilities.

Both attempts at improving the Q factor by removing the layer of adsorbed water failed. This is consistent with the silanols being the primary scatterer. To reverse these effects, a minimum temperature of 400°C[67] to remove all the vicinal silanols. Removing all the other, isolated, silanols would require temperature of over 1000°C. to do this, the mounts need to be fabricated with a material that does not deform or expand significantly between room temperature and the desired temperature. Alternatively, locally heating the SNAP such that the mount remains at room temperature could circumvent the issue of the mount deforming.

Chapter 7

Conclusion and Outlook

Despite SNAP's being a very promising platform due to their ultrahigh Q factor and easy of fabrication, there are still many issues inhibiting them from being used as in practical applications. The purpose of this thesis was to address some of these issues. The main results and future work is described below.

Radius and Refractive Index Measurement

A procedure was developed to measure the refractive index and radius which was applied to a SNAP. The measurement was not accurate because separation of variable could not describe the radius beyond 3 significant figures when 5 was need to reach the the standard deviation of the material's surface. This experiment could be redone on a WGR where separation of variables more accurately describes the system. Alternatively, a better theoretical model would allow measurements of the radius and refractive index.

Nanoparticle Carousel Induced Periodic Resonance Shift

As an example application of WGR, a nanoparticle carousel trap was set up in a hollow microbubble however, no periodic shift was observed due to the nanoparticle passing near the coupling region. If the effect was present, random fluctuations due to Brownian motion were too strong at low laser power. At higher power, the modes would not be stable enough due to what appears to be turbulence in the water.

Modes Locking

The Pound-Drever-Hall mode locking technique was review and applied to a fiber ring resonator. Locking to a cavity mode is useful for both detecting mode shifts with greater precision than with the transmission spectroscopy[] and for pumping consistent amounts of power into a mode[]. This will be useful in future experiments to very precisely measure resonance frequencies and will . In this chapter, we showed that a laser could be locked to a cavity with a Q factor of 10^8 using an inexpensive Red Pitaya$^{\text{TM}}$($\sim$ 350 USD) to replace the lock-in amplifiers, function generator and PID controller.

Packaging of Surface Nanoscale Axial Photonic Resonators

The packaging is adequate for research use but susceptible to breaking on impact.

The vacuum was high enough that most of the hydrogen bonded water was removed[67]. This is consistent with the hydrogen bonded water molecule not significantly reducing the Q factor and that the silanols must also be removed in restore the Q. which can be done by subjecting the SNAP to much higher temperatures.

Future Work

More work needs to be done to improving the model of the SNAP beyond separation of variables in order to properly measure the SNAP's radius and refractive index. Regardless of the this shortcoming, the procedure implies that the relative shift in resonances for orthogonal polarization is different for changes in refractive index compared to changes in radius. This difference is of linear order which implies that, by tracking both modes, a basis can be formed to sense two physical phenomena simultaneously.

More work needs to be done to observe the mode shift in the carousel experiment. Since the shift is thought to be caused by the tapered fiber perturbing the microbubble's mode, one possibility for our failure to observe the mode shift is that the taper may have been too small noticeable perturb or positioned to only weakly overlap with the mode. Some extra preparation may be able to produce a larger perturbation. Alternatively, the sensitivity can be improved by locking to the mode using the mode locking technique described in Chapter 5.

Some packaging could be engineered to better absorb the impact, however, it may not be worth improving because this design serves its purpose and the fabrication process is simple. For more robust applications like commercial products, other solutions have been proposed like coupling to photonic crystal silicon waveguides [68] or spot packaging[69], however, these are more complicated to fabricate. To remove the silanols from the silica surface, either a material with negligible deformation between room temperature and 400°C is required to restore the Q factor. Another option would be to locally heat the SNAP while leaving the packaging at room temperature.

This thesis contributed to by developing precise measurement techniques that may accurately determines the radius and refractive index of a SNAP given a accurate mode. Secondly, efforts were made to study the effects of a perturbation of the mode on a nanoparticle. Lastly, packaging was develop to improve robustness while trying to removing adsorbed water vapors that adsorb to the surface of silica.

Bibliography

1. Arumugam, M. Optical fiber communication—An overview. *Pramana* **57,** 849–869 (Nov. 1, 2001).
2. Collis, R. T. H. Lidar Observation of Cloud. *Science* **149,** 978–981 (Aug. 27, 1965).
3. Culshaw, B. The optical fibre Sagnac interferometer: an overview of its principles and applications. *Measurement Science and Technology* **17,** R1–R16 (Nov. 2005).
4. Zhang, X.-l., Ma, H.-l., Jin, Z.-h. & Ding, C. Open-loop operation experiments in a resonator fiber-optic gyro using the phase modulation spectroscopy technique. *Applied Optics* **45,** 7961–7965 (Nov. 1, 2006).
5. Ludlow, A. D., Boyd, M. M., Ye, J., Peik, E. & Schmidt, P. O. Optical atomic clocks. *Reviews of Modern Physics* **87,** 637–701 (June 26, 2015).
6. Galdino, L. *et al.* Optical Fibre Capacity Optimisation via Continuous Bandwidth Amplification and Geometric Shaping. *IEEE Photonics Technology Letters* **32,** 1021–1024 (Sept. 2020).
7. Fürst, J. U. *et al.* Naturally Phase-Matched Second-Harmonic Generation in a Whispering-Gallery-Mode Resonator. *Physical Review Letters* **104,** 153901 (Apr. 12, 2010).
8. Del'Haye, P. *et al.* Optical frequency comb generation from a monolithic microresonator. *Nature* **450,** 1214–1217 (Dec. 2007).
9. Arnold, S. *et al.* Whispering gallery mode carousel – a photonic mechanism for enhanced nanoparticle detection in biosensing. *Opt. Express, OE* **17,** 6230–6238 (Apr. 13, 2009).

10. Ward, J. M., Yang, Y. & Chormaic, S. N. *Nanoparticle trapping and control in a hollow whispering gallery resonator* in *Optical Manipulation Conference* Optical Manipulation Conference. **10252** (International Society for Optics and Photonics, Apr. 18, 2017).

11. Spillane, S. M., Kippenberg, T. J. & Vahala, K. J. Ultralow-threshold Raman laser using a spherical dielectric microcavity. *Nature* **415,** 621–623 (Feb. 2002).

12. Grudinin, I. S., Matsko, A. B. & Maleki, L. Brillouin Lasing with a ${\mathrm{CaF}}_{2}$ Whispering Gallery Mode Resonator. *Physical Review Letters* **102,** 043902 (Jan. 28, 2009).

13. Li, B.-B. *et al.* On chip, high-sensitivity thermal sensor based on high-Q polydimethylsiloxane-coated microresonator. *Applied Physics Letters* **96,** 251109 (June 21, 2010).

14. Dong, C.-H. *et al.* Fabrication of high-Q polydimethylsiloxane optical microspheres for thermal sensing. *Applied Physics Letters* **94,** 231119 (June 8, 2009).

15. Martín, L. L., Pérez-Rodríguez, C., Haro-González, P. & Martín, I. R. Whispering gallery modes in a glass microsphere as a function of temperature. *Optics Express* **19,** 25792–25798 (Dec. 5, 2011).

16. Ward, J. M., Dhasmana, N. & Nic Chormaic, S. Hollow core, whispering gallery resonator sensors. *The European Physical Journal Special Topics* **223,** 1917–1935 (Sept. 1, 2014).

17. Ioppolo, T. & Ötügen, M. V. Pressure tuning of whispering gallery mode resonators. *JOSA B* **24,** 2721–2726 (Oct. 1, 2007).

18. Henze, R., Seifert, T., Ward, J. & Benson, O. Tuning whispering gallery modes using internal aerostatic pressure. *Optics Letters* **36,** 4536–4538 (Dec. 1, 2011).

19. Bogatyrev, V. A. *et al.* Change in the spectrum of optical whispering-gallery modes in a quasi-cylindrical microresonator caused by an acoustic pressure pulse. *Quantum Electronics* **32,** 471 (June 30, 2002).

20. Yang, Y., Saurabh, S., Ward, J. M. & Chormaic, S. N. High-Q, ultrathin-walled microbubble resonator for aerostatic pressure sensing. *Opt. Express, OE* **24,** 294–299 (Jan. 11, 2016).

21. Liang, W. *et al.* Resonant microphotonic gyroscope. *Optica* **4,** 114–117 (Jan. 20, 2017).

22. Li, J., Suh, M.-G. & Vahala, K. Microresonator Brillouin gyroscope. *Optica* **4,** 346–348 (Mar. 20, 2017).

23. Lai, Y.-H., Lu, Y.-K., Suh, M.-G., Yuan, Z. & Vahala, K. Observation of the exceptional-point-enhanced Sagnac effect. *Nature* **576,** 65–69 (Dec. 2019).

24. Ward, J. M. *et al.* Nanoparticle sensing beyond evanescent field interaction with a quasi-droplet microcavity. *Optica* **5,** 674–677 (June 20, 2018).

25. Vollmer, F., Arnold, S. & Keng, D. Single virus detection from the reactive shift of a whispering-gallery mode. *Proceedings of the National Academy of Sciences* **105,** 20701–20704 (Dec. 30, 2008).

26. Vollmer, F. *et al.* Protein detection by optical shift of a resonant microcavity. *Applied Physics Letters* **80,** 4057–4059 (May 20, 2002).

27. Ali, A. R., Ioppolo, T., Ötügen, V., Christensen, M. & MacFarlane, D. Photonic electric field sensor based on polymeric microspheres. *Journal of Polymer Science Part B: Polymer Physics* **52,** 276–279 (2014).

28. Ioppolo, T. & Ötügen, M. V. Magnetorheological polydimethylsiloxane microoptical resonator. *Optics Letters* **35,** 2037–2039 (June 15, 2010).

29. Ma, Q., Huang, L., Guo, Z. & Rossmann, T. Spectral shift response of optical whispering-gallery modes due to water vapor adsorption and desorption. *Measurement Science and Technology* **21,** 115206 (Oct. 2010).

30. Yebo, N. A., Lommens, P., Hens, Z. & Baets, R. An integrated optic ethanol vapor sensor based on a silicon-on-insulator microring resonator coated with a porous ZnO film. *Optics Express* **18,** 11859–11866 (May 24, 2010).

31. Robinson, J. T., Chen, L. & Lipson, M. On-chip gas detection in silicon optical microcavities. *Optics Express* **16,** 4296–4301 (Mar. 17, 2008).

32. Ksendzov, A., Homer, M. L. & Manfreda, A. M. Integrated optics ring-resonator chemical sensor with polymer transduction layer. *Electronics Letters* **40,** 63–65 (Jan. 8, 2004).

33. Bajcsy, M. *et al.* Efficient All-Optical Switching Using Slow Light within a Hollow Fiber. *Physical Review Letters* **102,** 203902 (May 18, 2009).

34. Tucker, R. S., Ku, P.-C. & Chang-Hasnain, C. J. Slow-Light Optical Buffers: Capabilities and Fundamental Limitations. *Journal of Lightwave Technology* **23,** 4046 (Dec. 1, 2005).

35. Lvovsky, A. I., Sanders, B. C. & Tittel, W. Optical quantum memory. *Nature Photonics* **3,** 706–714 (Dec. 2009).

36. Louyer, Y., Meschede, D. & Rauschenbeutel, A. Tunable whispering-gallery-mode resonators for cavity quantum electrodynamics. *Physical Review A* **72,** 031801 (Sept. 15, 2005).

37. Bianucci, P. Optical Microbottle Resonators for Sensing. *Sensors* **16,** 1841 (Nov. 2016).

38. Oraevsky, A. N. Whispering-gallery waves. *Quantum Electron.* **32,** 377 (2002).

39. Zangwill, A. *Modern Electrodynamics* 1005 pp. (Cambridge University Press, 2013).

40. Gorodetsky, M. L., Savchenkov, A. A. & Ilchenko, V. S. Ultimate Q of optical microsphere resonators. *Opt. Lett., OL* **21,** 453–455 (Apr. 1, 1996).

41. Snyder, A. & Love, J. Reflection at a Curved Dielectric Lnterface - Electromagnetic Tunneling. *IEEE Transactions on Microwave Theory and Techniques* **23,** 134–141 (Jan. 1975).

42. Schwinger, J., Jr, L. L. D., Milton, K. & Tsai, W.-y. *Classical Electrodynamics* 594 pp. (Avalon Publishing, Sept. 11, 1998).

43. Cai, L., Pan, J. & Hu, S. Overview of the coupling methods used in whispering gallery mode resonator systems for sensing. *OPT LASER ENG* **127,** 105968 (Apr. 1, 2020).

44. Cai, M. & Vahala, K. Highly efficient optical power transfer to whispering-gallery modes by use of a symmetrical dual-coupling configuration. *Optics Letters* **25,** 260–262 (Feb. 15, 2000).

45. Cao, Z. & Yin, C. in *Advances in One-Dimensional Wave Mechanics: Towards A Unified Classical View* (eds Cao, Z. & Yin, C.) 1–14 (Springer, Berlin, Heidelberg, 2014).

46. Rowland, D. & Love, J. Evanescent wave coupling of whispering gallery modes of a dielectric cylinder. *IEE Proceedings J - Optoelectronics* **140,** 177–188 (June 1993).

47. Stokes, L. F., Chodorow, M. & Shaw, H. J. All-single-mode fiber resonator. *Optics Letters* **7,** 288–290 (June 1, 1982).

48. Sumetsky, M. & Dulashko, Y. Radius variation of optical fibers with angstrom accuracy. *Optics Letters* **35,** 4006–4008 (Dec. 1, 2010).

49. Birks, T. A., Knight, J. C. & Dimmick, T. E. High-resolution measurement of the fiber diameter variations using whispering gallery modes and no optical alignment. *IEEE Photonics Technology Letters* **12,** 182–183 (Feb. 2000).

50. Bilodeau, F., Hill, K. O., Faucher, S. & Johnson, D. C. *Low-loss highly overcoupled fused couplers: Fabrication and sensitivity to external pressure* in *Optical Fiber Sensors (1988), paper ThCC10* Optical Fiber Sensors (Optical Society of America, Jan. 27, 1988), ThCC10.

51. Birks, T. & Li, Y. The shape of fiber tapers. *Journal of Lightwave Technology* **10,** 432–438 (Apr. 1992).

52. Sumetsky, M. Nanophotonics of optical fibers. *Nanophotonics* **2,** 393–406 (Dec. 16, 2013).

53. Hamidfar, T. *Fabrication and characterization of surface nanoscale axial photonics microresonators* masters (Concordia University, Apr. 15, 2015). 123 pp.

54. Hamidfar, T. private communication. July 2018.

55. Ashkin, A. Acceleration and Trapping of Particles by Radiation Pressure. *Phys. Rev. Lett.* **24,** 156–159 (Jan. 26, 1970).

56. Ashkin, A. & Dziedzic, J. M. Optical Levitation by Radiation Pressure. *Applied Physics Letters* **19,** 283–285 (Oct. 15, 1971).

57. Ashkin, A., Dziedzic, J. M., Bjorkholm, J. E. & Chu, S. Observation of a single-beam gradient force optical trap for dielectric particles. *Optics Letters* **11,** 288–290 (May 1, 1986).

58. Ward, J. private communication. July 2019.

59. Arnold, S., Ramjit, R., Keng, D., Kolchenko, V. & Teraoka, I. MicroParticle photophysics illuminates viral bio-sensing. *Faraday Discuss.* **137,** 65–83 (Oct. 16, 2008).

60. Keng, D., McAnanama, S. R., Teraoka, I. & Arnold, S. Resonance fluctuations of a whispering gallery mode biosensor by particles undergoing Brownian motion. *Applied Physics Letters* **91,** 103902 (Sept. 3, 2007).

61. Drever, R. W. P. *et al.* Laser phase and frequency stabilization using an optical resonator. *Appl. Phys. B* **31,** 97–105 (June 1, 1983).

62. Black, E. D. An introduction to Pound–Drever–Hall laser frequency stabilization. *American Journal of Physics* **69,** 79–87 (Dec. 15, 2000).

63. Bjorklund, G. C., Levenson, M. D., Lenth, W. & Ortiz, C. Frequency modulation (FM) spectroscopy. *Appl. Phys. B* **32,** 145–152 (Nov. 1, 1983).

64. Day, T., Gustafson, E. & Byer, R. Sub-hertz relative frequency stabilization of two-diode laser-pumped Nd:YAG lasers locked to a Fabry-Perot interferometer. *IEEE Journal of Quantum Electronics* **28,** 1106–1117 (Apr. 1992).

65. Luda, M. A., Drechsler, M., Schmiegelow, C. T. & Codnia, J. Compact embedded device for lock-in measurements and experiment active control. *Review of Scientific Instruments* **90,** 023106 (Feb. 2019).

66. Zhang, S., Li, G., Lin, L. & Zhao, J. Optimization of a digital lock-in algorithm with a square-wave reference for frequency-divided multi-channel sensor signal detection. *Review of Scientific Instruments* **87,** 085102 (Aug. 1, 2016).

67. Zhuravlev, L. The surface chemistry of amorphous silica. Zhuravlev model. *Colloids and Surfaces A: Physicochemical and Engineering Aspects* **173,** 1–38 (Nov. 2000).

68. Zhuang, Y. *et al.* Coupling of a whispering gallery mode to a silicon chip with photonic crystal. *Optics Letters* **44,** 5731–5734 (Dec. 1, 2019).

69. Yan, Y. *et al.* Robust Spot-Packaged Microsphere-Taper Coupling Structure for In-Line Optical Sensors. *IEEE Photonics Technology Letters* **23,** 1736–1738 (Nov. 2011).